Rogue Waves on a Vortex Filament

Rehan Shah

St Anne's College

University of Oxford

A dissertation submitted for the degree of

Master of Science in Mathematical Modelling and Scientific Computing

Trinity 2015

To my Parents and Brother

for their unending support and encouragment

Acknowledgements

I would like to thank Dr. Robert Van Gorder for his valuable insights, encouragement and guidance as my supervisor throughout the course of this project. Finally, I would also like to thank my family, friends and Kathryn for all their support, faith and interest during the preparation of this dissertation.

Abstract

The presence of a standing soliton on a vortex filament has been demonstrated theoretically by Hasimoto [1] for classical fluids, by Van Gorder [2] for quantum fluids as well as experimentally by Hopfinger and Browand [3] for turbulent flow in a rotating container. This was done by mapping solutions of the local induction approximation (LIA) governing the motion of a thin vortex filament to those of nonlinear scalar PDEs such as the cubic nonlinear Schrödinger equation (NLS) and the complex Ginsburg-Landau equation (GLE) using the Hasimoto transformation and its recently developed quantum analogue.

Unlike solitons that maintain a constant shape over time, rogue waves are another class of solutions to the NLS, that possess greater variability in their shape and can thus be used to study the propagation of temporary disturbances along vortex filaments. The purpose of this dissertation is therefore to study the formation and propagation of such rogue waves along vortex filaments in both classical and quantum fluids. This has not been done previously in the presence of quantum effects such as mutual friction and a coupled normal fluid flow.

While rogue waves have recently been observed experimentally in water tanks [4], models such as the Peregrine soliton [5] and the more generalised Akhmediev breather wave [6] have also been investigated as solutions of the NLS in previous literature. By employing the Hasimoto transformation as done for solitons, LIA solutions for the motion of both classical and quantum vortex filament solutions are obtained for complex rogue wave models such as breathers.

It is found that the solutions obtained do indeed demonstrate the transient behaviour that is typically associated with rogue waves, particularly as the vortex filament transitions from the classical to the quantum regime. The results obtained not only shed light on the emergence of highly localised asymptotically-decaying disturbances along vortex filaments, but also bear significant implications for the onset of quantum turbulence and chaotic motion in superfluids.

Contents

Nomenclature

Vortex Filament Model

$\mathbf{b}$	unit binormal vector
$\mathbf{n}$	unit normal vector
$\mathbf{r}(s,t)$	position vector of the filament
s	arclength
t	time
$\mathbf{t}$	unit tangential vector
$\mathbf{U}$	normal fluid velocity
$\mathbf{v}(s,t)$	velocity of the filament
α, α'	mutual friction parameters
$\kappa(s,t)$	curvature of the filament
$\tau(s,t)$	torsion of the filament

Hasimoto Map

$A(t)$	arbitrary function of time
$\mathbf{m}$	vector valued function
$\phi(s,t)$	real valued function
$\psi(s,t)$	complex variable function $\psi : \mathbb{R}^2 \mapsto \mathbb{C}$

Inverse Map

$\mathcal{A}(s,t), \mathcal{M}(s,t)$	curvature-torsion variable matrices
$\mathbf{C}(t)$	constant time-dependent matrix
$\mathcal{Q}(s,t)$	matrix exponential
$\mathbf{W}(s,t)$	row vector of unit tangential, normal and binormal vectors
$\mathbf{W}_1(s,t), \mathbf{W}_2(s,t), \mathbf{W}_3(s,t)$	component vectors corresponding to each unit vector

$\mathbf{U} \neq \mathbf{0}$ Map

U_1, U_2, U_3	components of normal fluid velocity vector $\mathbf{U}$ in y, z and x directions
$v(s,t)$	complex variable function $v : \mathbb{R}^2 \mapsto \mathbb{C}$

List of Figures

Chapter 1

Introduction

The motion of vortex filaments in two dimensions has been extensively documented in the literature, however the three-dimensional motion presents additional degrees of complexity due to the non-local Biot-Savart dynamics governing the motion. This necessitated the formulation of an equation to approximate the local motion of a thin vortex filament, which was presented by Batchelor in his 1967 book [8] in the form of the local induction approximation (LIA), an asymptotic theory formulated by Da Rios [9] in 1906.

The LIA captures the local dynamics of a vortex filament by relating its velocity to its curvature, with the help of the unit tangential and normal vectors at any point on the filament. The ingenious essence of this method lies in the fact that the motion of the vortex filament in the x, y and z directions can be determined completely if both the curvature κ and torsion τ of the filament are known. Besides the fact that there is a reduction in the number of unknown quantities to compute, this mapping also heralds the transition from the more complicated vector problem to a simpler scalar representation of the same problem.

1.1 Classical Hasimoto 1-Soliton

Hasimoto, in his 1972 paper [1] developed a transformation for classical fluids that mapped a three-dimensional vector LIA equation to a scalar PDE, the cubic nonlinear

Schrödinger equation (NLS). The map transforms the vector equation

$$\mathbf{v} = \kappa\, \mathbf{t} \times \mathbf{n}, \tag{1.1}$$

into the complex scalar equation

$$\dot{\psi} = i\psi_{ss} + \left(\frac{i}{2}\right)|\psi|^2\psi, \tag{1.2}$$

where $\mathbf{v}(s,t) = \mathbf{r}_t(s,t)$ is the velocity of the filament as a function of arclength s and time t, κ is the curvature and $\mathbf{t}$ and $\mathbf{n}$ are the unit tangential and normal vectors respectively. Throughout this dissertation, the dot symbol $\dot{(\,)}$ is used to denote the derivative of a quantity with respect to time $\partial/\partial t$. The definition of the complex variable $\psi(s,t)$ in Equation (1.3)

$$\psi(s,t) = \kappa(s,t)\, \mathrm{e}^{i\int_0^s \tau(\hat{s},t)\mathrm{d}\hat{s}}, \tag{1.3}$$

encapsulates both the curvature and torsion of the filament with the former as its amplitude and the latter as its phase.

This results in a solution describing a sech-type of stationary solitary wave that propagates spatially along the vortex filament, while retaining a constant shape over time. The curvature of the filament at every time step yields a symmetric envelope that reaches its peak amplitude at the origin and tends to zero at either end of the filament as shown by the zero-temperature curve in Figure 1.1. Since its form is characterised by a single bump, this type of solution is termed as a stationary 1-soliton. The torsion of the filament, for the classical case, is found to be zero, while implies that the filament does not exhibit any twisting motion. Hasimoto [1] concludes by re-mapping the curvature-torsion solutions to obtain the three-dimensional position vector $\mathbf{r}(s,t)$ of the vortex filament, which facilitates the complete construction of the curve of the filament in space and time.

1.2 Quantum Hasimoto 1-Soliton

The classical case considered by Hasimoto [1] neglects temperature-dependent friction parameters by assuming a zero-temperature limit. However, in his 2015 paper, Van Gorder [2] recently developed a quantum analogue for the Hasimoto transformation

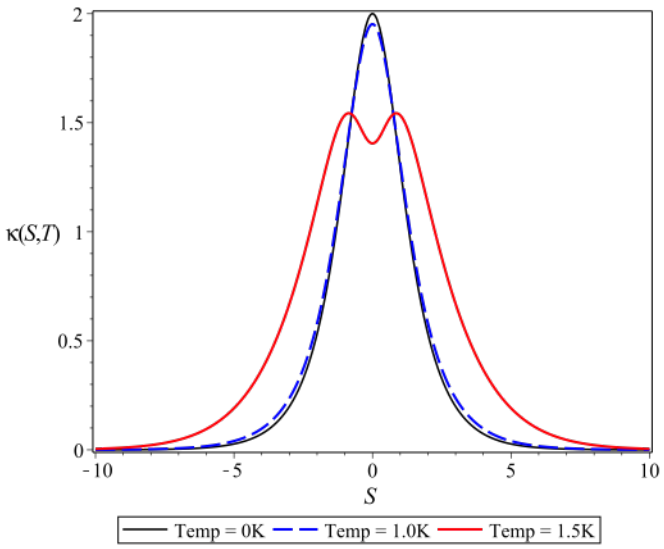

Figure 1.1: Plot of vortex filament curvature for classical and quantum solitons with varying temperature (Source: Van Gorder [2]).

to describe the motion of a thin vortex filament in quantum fluids such as superfluid helium-4. The paper maps the quantum LIA derived by Schwarz [10] that accounts for both mutual friction occurring at finite temperatures and the interaction of the filament with a normal fluid to a scalar PDE, a complex Ginsberg-Landau equation (GLE) with an extra dissipation term. The map transforms the vector equation

$$\mathbf{v} = \kappa\,\mathbf{t}\times\mathbf{n} + \alpha\,\mathbf{t}\times(\mathbf{U} - \kappa\,\mathbf{t}\times\mathbf{n}) - \alpha'\,\mathbf{t}\times(\mathbf{t}\times(\mathbf{U} - \kappa\,\mathbf{t}\times\mathbf{n})), \tag{1.4}$$

into the complex scalar equation

$$\begin{aligned}\dot{\psi} = iA(t)\psi + (i(1-\alpha') + \alpha)\psi_{ss} + \left(\frac{i(1-\alpha')}{2} - \alpha\right)|\psi|^2\psi \\ - \frac{\alpha}{2}\psi\int_0^s \{\psi(\hat{s},t)\psi_s(\hat{s},t)^* - \psi(\hat{s},t)^*\psi_s(\hat{s},t)\}\mathrm{d}\hat{s},\end{aligned} \tag{1.5}$$

where α and α' are the mutual friction parameters, $\mathbf{U}$ is the dimensionless normal fluid velocity and $A(t)$ is an arbitrary function of time. For $\alpha, \alpha' = 0$, Equation (1.5) reduces to the cubic NLS obtained by Hasimoto [1]. However, the GLE equation is obtained by assuming that the normal fluid velocity effects are small enough to be neglected with $\mathbf{U} = O(\alpha)$ (so that $\alpha\mathbf{U} = O(\alpha^2)$).

Using the definition of $\psi(s,t)$ given in Equation (1.3), the quantum case results in a solution describing a sech $+O(\alpha)$-type of pertubed first-order soliton that propagates

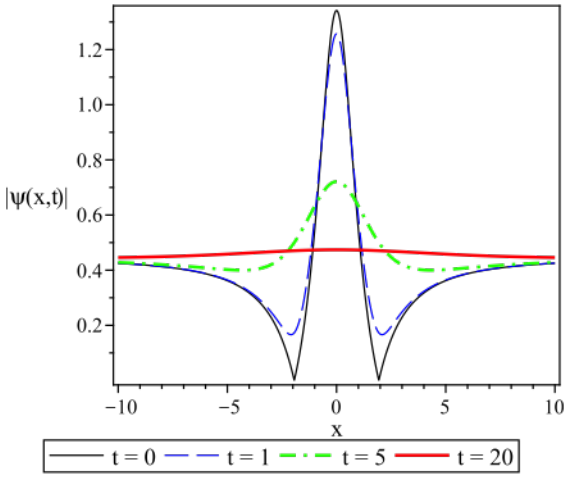

Figure 1.2: Time evolution of the Peregrine soliton behaving as a rogue wave (Source: Van Gorder [5]).

spatially along the vortex filament, while retaining a constant shape over time. The curvature of the filament at every time step yields a symmetric envelope that reaches its peak amplitude at the origin and tends to zero at either end of the filament as shown by the finite temperature curves in Figure 1.1. As the temperature increases though, rapid decay of the curvature results in a double hump at the origin. In this case however, the torsion does depend on the arclength s to reach large values at the ends of the filament, only to become minimal near the origin. The filament, thus assumes the shape of a line at values sufficiently far from the origin.

Van Gorder [2] concludes by noting that gradual dissipative effects on the amplitude of the soliton, influenced by the spatial variation of the torsion of the filament curve, occur at $O(\alpha^2)$ or higher, which is slow enough to enable the experimental verification of solitons on quantum vortex filaments at low temperatures. An essential assumption made in the derivation of the quantum Hasimoto transformation in [2] is that the effects of normal fluid velocity are neglected, though this still does not detract from the physical relevance of the solutions, especially in the low-temperature regime.

The primary question that this dissertation investigates is whether rogue wave models such as the Peregrine soliton [5] in Figure 1.2 as well as generalised breather waves such as the Akhmediev breather wave [6], as solutions of the NLS, can be used to obtain LIA solutions that can describe the motion of vortex filaments in three dimensions. The crucial aspect that differentiates rogue waves from the soliton solutions obtained in the literature is their spatial variability over time that is to

say, as highly localised phenomenon, rogue waves decay asymptotically over time and are also orbitally unstable [5].

1.3 Implications for Quantum Turbulence

The stochastical dynamics of vortex filaments, particularly in quantum fluids, possesses significant potential to aid in the understanding of superfluid turbulence, a term coined by Feynman in 1955 [11]. This describes the appearance of a disordered set of quantised vortex lines termed vortex tangles in superfluids such as He II for velocity values above a critical value [12].

Quantum turbulence is an active area of current research and spans several related areas as part of the theory of superfluidity including vortex generation, interaction and reconnection of closely spaced vortex lines and phase transition problems influenced by quantum vortices [13]. Characterised by highly disordered sets of one-dimensional singularities and defects, the theory of superfluid turbulence is also perceived to be a variation of string field theory as it is used in the study of chaotic motion of objects possessing nonlinear and non-local interactions and reconnections.

What is interesting to note is that equations such as the Biot-Savart Law describing the non-local dynamics of vortex-line motion provide valuable information about the properties of vortex tangles, which in turn form the essence of quantum turbulence. The complexity of this problem originates from the coupling of the deterministic motion of the vortex filaments and random collisions of the vortex loops, which motivates the reduction of the Biot-Savart model to a simpler local induction approximation (LIA) model discussed in Section 2.2 in Chapter 2 that culminates with the cubic NLS equation.

The small deformations of vortex lines are referred to as Kelvin waves [14], which serve as the primary mechanism to account for the low temperature decay of superfluid turbulence in the absence of dissipation through mutual friction. The appearance of large vortex rings in chaotic quantised vortices in He II aids in shedding further light on phase transition problems. The key question "To what extent is the dynamics of a set of vortex line able to reproduce the properties of real hydrodynamic turbulence?" [13] can thus be answered by studying the behaviour of vortex filaments not in classical fluids, but in quantum fluids.

1.4 Practical Applications

The study of nonlinear rogue wave models such as solitons and breathers has been a subject of active research for quite some time and this can largely be attributed to the prevalence of such waves in a wide range of practical applications. Solitons have traditionally been used as models to study natural disasters such as tsunamis in oceans [15]. While dark solitons have led to the generation of quantised vortices through the snake instability described in [16], bright solitons have found great use in nonlinear optics [17].

The study of breather solutions has not been as frequent as that of solitons, yet they have been observed in a wide range of interesting scenarios. Rogue waves observed experimentally in water tanks [4] were found to closely resemble the Peregrine soliton, which has also found use in optical fibres [18], Bose-Einstein condensates [19] and plasmas [20]. However, rogue waves have not been studied extensively in the context of vortex dynamics, which is what this dissertation endeavours to achieve.

1.5 Organisation of the Thesis

The following provides a brief summary of the organisation of the chapters in this dissertation. A model-based approach is adopted in which rogue wave solutions for the classical case are analysed first, before moving on to the more complicated quantum case, which accounts for the effects of both mutual friction and normal fluid velocity. Chapter 2 begins by presenting classical solutions for both the Peregrine soliton and Akhmediev breather using the Hasimoto transformation to determine curvature and torsion solutions from the LIA equation. The analysis is then extended in Chapter 3 to the quantum case with $\mathbf{U} = \mathbf{0}$, where an attempt is made to use a regular pertubation of the Hasimoto map to obtain solutions for rogue waves on quantum vortex filaments. Solutions for the quantum Peregrine soliton and Akhmediev breather subject to normal fluid velocity effects are described in Chapter 4, after employing a pertubation approach on the new model developed. Finally, the physical relevance of the solutions obtained and their implications for the interaction and reconnection of vortex filaments in quantum turbulence are discussed in Chapter 5. Chapter 6 outlines the principal findings of the study, along with their impact on the field of vortex dynamics and also suggests ideas for future extensions to the work.

Chapter 2

Classical Model

2.1 Definitions

It is useful to introduce the definitions for some of the principal terminology that form the core of this dissertation:

- **Solitary Wave**: A solitary wave can be described as a localised "wave of translation" [21] that propagates without any temporal evolution in its shape or size, arising due to the cancellation of nonlinearity and dispersion effects. It thus maintains its form when it moves at constant velocity and decays or tends to a constant value at infinity.
- **Soliton**: A soliton is a nonlinear solitary wave, possessing the additional particle-like property that enables it to retain its structure and emerge unchanged, even after interacting with another soliton [22]. This term is also more commonly used to describe multiple solutions of weakly nonlinear dispersive PDEs such as the Korteweg-de Vries (KdV) equation, the sine-Gordon equation and the NLS equation stated in Chapter 1.
- **Rogue Wave**: A rogue wave also known as a freak wave, corresponds to a large-amplitude wave appearing unexpectedly on the sea-surface as an "open water phenomenon", whose height exceeds at least twice that of the significant wave height [23].
- **Breather**: A breather is a nonlinear wave used to describe localised, oscillatory solutions of integrable models such as the sine-Gordon equation and the NLS

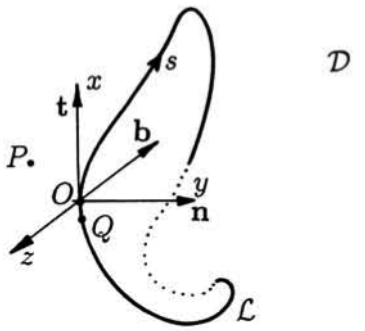

Figure 2.1: Local motion of a thin isolated vortex filament (Source: Ricca [7]).

that demonstrate both spatial and temporal variations [24]. The simplest example of a breather as a solution of the NLS is the Peregrine soliton which is a special limiting case of the spatially-periodic Akhmediev breather solution.

2.2 Vortex Filament LIA Model

The self-induced motion of thin vortex filaments in three dimensions is best described in its exact form by the Biot-Savart integral stated in [25] as

$$\mathbf{v} = -\frac{\Gamma}{4\pi} \int_{\mathcal{L}} |\mathbf{r}|^{-3} \frac{\partial \mathbf{r}}{\partial s} \times \mathbf{r}\, ds, \tag{2.1}$$

where $\mathbf{r}(s,t)$, as a function of arclength s and time t, corresponds to the relative position vector between points P and Q from Figure 2.1, while Γ denotes the strength of the vortex. The point P represents an external point in an infinite domain $\mathcal{D}$ in $\mathbb{R}^3$ of the incompressible, inviscid fluid, while Q is a point lying on the vortex filament $\mathcal{L}$. The vectors $\mathbf{t}$, $\mathbf{n}$ and $\mathbf{b} = \mathbf{t} \times \mathbf{n}$ correspond to the unit tangential, normal and binormal vectors respectively.

A major mathematical difficulty posed by the evaluation of the Biot-Savart integral was the logarithmic singularity encountered as $|\mathbf{r}|$ approached 0, leading to divergence of the integral and preclusion of an analytical solution. On recognising this problem, Da Rios in his 1906 thesis [9], developed an asymptotic model known as localised induction approximation (LIA) that enabled determination of the induced velocity in thin vortex filaments for the limiting case of an infinitesimal core size and negligible long-distance contributions from distant parts and self-interaction.

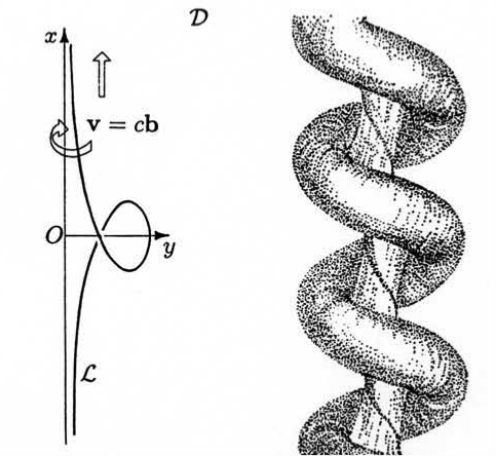

Figure 2.2: Loop generated vortex surface swept out by the helical motion of the Hasimoto soliton (Source: Ricca [7]).

The key steps in the derivation of the LIA expression as outlined by Arms and Hama in [25] are presented below. The relative position vector

$$\mathbf{r}(\xi, t) = \mathbf{r}_P(s, t) - \mathbf{r}_Q(s + \xi, t), \tag{2.2}$$

can be expanded as a Taylor series for a small parameter ξ as

$$\mathbf{r}(\xi) = \mathbf{a}_1\xi + \mathbf{a}_2\xi^2 + \ldots, \tag{2.3}$$

where

$$\mathbf{a}_1 = \partial\mathbf{r}/\partial\xi, \quad \mathbf{a}_2 = \frac{1}{2}\partial^2\mathbf{r}/\partial\xi^2, \ldots \quad \text{at } \xi = 0. \tag{2.4}$$

Assuming that the curve is smooth so that its derivatives exist implies that

$$\partial\mathbf{r}/\partial s = \partial\mathbf{r}/\partial\xi = \mathbf{a}_1 + 2\mathbf{a}_2\xi + \ldots, \tag{2.5}$$

and

$$\begin{aligned} -\partial\mathbf{r}/\partial s \times \mathbf{r} &= (\mathbf{a}_1\xi + \mathbf{a}_2\xi^2 + \ldots) \times (\mathbf{a}_1 + 2\mathbf{a}_2\xi + \ldots) \\ &= (\mathbf{a}_1 \times \mathbf{a}_1)\xi + ((\mathbf{a}_2 \times \mathbf{a}_1 + 2\mathbf{a}_1 \times \mathbf{a}_2)\xi^2 + O(\xi^3) \\ &= (\mathbf{a}_1 \times \mathbf{a}_2)\xi^2 + O(\xi^3) \\ &= (\mathbf{a}_1 \times \mathbf{a}_2)|\xi^2|. \end{aligned} \tag{2.6}$$

On the other hand,

$$|\mathbf{r}|^2 = |(\mathbf{a}_1\xi + \mathbf{a}_2\xi^2 + \ldots)^2|, \tag{2.7}$$

$$|\mathbf{r}| = |\mathbf{a}_1||\xi|\left(1 + \frac{\mathbf{a}_1 \cdot \mathbf{a}_2}{|\mathbf{a}_1|^2}\xi + \ldots\right), \tag{2.8}$$

$$|\mathbf{r}|^{-3} = |\mathbf{a}_1|^{-3}|\xi|^{-3}\left(1 - 3\frac{\mathbf{a}_1 \cdot \mathbf{a}_2}{|\mathbf{a}_1|^2}\xi + \ldots\right). \tag{2.9}$$

Substituting the terms above into the Biot-Savart expression (2.1) yields

$$\mathbf{v} = \frac{\Gamma}{4\pi}\int\left[\frac{\mathbf{a}_1 \times \mathbf{a}_2}{|\mathbf{a}_1|^3}\frac{1}{|\xi|} + O(1)\right]d\xi, \tag{2.10}$$

which when integrated over the limits $\epsilon \leq |\xi| \leq 1$ results in

$$\mathbf{v} = \frac{\Gamma}{4\pi}\left[\log\left(\frac{1}{\epsilon}\right) + O(1)\right]\frac{\mathbf{a}_1 \times \mathbf{a}_2}{|\mathbf{a}_1|^3}. \tag{2.11}$$

Using the definition for $\mathbf{a}_1$ and $\mathbf{a}_2$ from (2.4), this can be rewritten as

$$\mathbf{v} = \frac{\Gamma}{4\pi}\left[\log\left(\frac{1}{\epsilon}\right) + O(1)\right]\frac{(\partial\mathbf{r}/\partial s) \times \partial^2\mathbf{r}/\partial s^2}{|\partial\mathbf{r}/\partial s|^3}. \tag{2.12}$$

Making use of the Frenet-Serret formulae $\mathbf{t} = \partial\mathbf{r}/\partial s$, $\mathbf{n} = \kappa^{-1}\,\partial^2\mathbf{r}/\partial s^2$, this simplifies to the dimensionalised version of the LIA relation stated in (1.1) in Chapter 1

$$\mathbf{v} = G\kappa\,\mathbf{t} \times \mathbf{n} = G\kappa\,\mathbf{b}, \tag{2.13}$$

where κ is the curvature of the vortex filament and $G = (\Gamma/4\pi)\left[\log(1/\epsilon) + O(1)\right]$ is the coefficient of local induction.

A complete description of the motion of the vortex filament can be equivalently obtained by determining both curvature $\kappa(s,t)$ and torsion $\tau(s,t)$ in the scalar regime to re-map them back to the position vector $\mathbf{r} = (x(s,t), y(s,t), z(s,t))$ in three dimensions.

A schematic of a loop generated vortex surface swept out by the Hasimoto soliton [1] with $\mathbf{v} = c\mathbf{b}$ and torsion $\tau =$ constant $\neq 0$ is shown in Figure 2.2.

2.3 Hasimoto Map: $\{\mathbf{r}(s,t)\} \mapsto \{\kappa(s,t), \tau(s,t)\}$

The mathematical formulation for the classical Hasimoto map is reproduced entirely from [1] in this section as the fundamental tool used to obtain solutions to the classical LIA equation

$$\mathbf{v} = \kappa\, \mathbf{t} \times \mathbf{n}. \tag{2.14}$$

The Frenet-Serret formulae $\mathbf{t}_s = \kappa\mathbf{n}$, $\mathbf{n}_s = -\kappa\mathbf{t} + \tau\mathbf{b}$ and $\mathbf{b}_s = -\tau\mathbf{n}$ are used to yield

$$\dot{\mathbf{t}} = (\kappa\mathbf{b})_s, \tag{2.15}$$

where the dot symbol denotes derivative with respect to time.

The complex variable $\psi(s,t)$ is defined below in a way that it contains information about both curvature and torsion as the real and imaginary parts respectively that is,

$$\psi(s,t) = \kappa(s,t)\, \mathrm{e}^{i\int_0^s \tau(\hat{s},t)\mathrm{d}\hat{s}}. \tag{2.16}$$

The idea behind the approach that follows is to obtain a partial differential equation, which can be solved for the variable $\psi(s,t)$, in order to determine both curvature and torsion. On prescribing a new vector-valued function $\mathbf{m} = (\mathbf{n} + i\mathbf{b})\mathrm{e}^{i\int_0^s \tau(\hat{s},t)\mathrm{d}\hat{s}}$, the quantities $\mathbf{m}_s = -\psi\mathbf{t}$, $\mathbf{t}_s = \frac{1}{2}(\psi^*\mathbf{m} + \psi\mathbf{m}^*)$ and $(\kappa\mathbf{b})_s = \frac{i}{2}(\psi_s\mathbf{m}^* - \psi_s^*\mathbf{m})$, where $*$ denotes complex conjugation, are computed. The classical LIA can then be written as

$$\dot{\mathbf{t}} = \frac{i}{2}(\psi_s\mathbf{m}^* - \psi_s^*\mathbf{m}). \tag{2.17}$$

In a similar manner as done by Hasimoto [1], it is worth noting that

$$\dot{\mathbf{m}}_s = -\dot{\psi}\mathbf{t} - \psi\dot{\mathbf{t}} = -\dot{\psi}\mathbf{t} + \frac{i}{2}\psi\psi_s^*\mathbf{m} - \frac{i}{2}\psi\psi_s\mathbf{m}^*. \tag{2.18}$$

An equivalent expression for $\mathbf{m}_s$ is then obtained by first representing $\dot{\mathbf{m}}$ in the form

$$\dot{\mathbf{m}} = a\mathbf{m} + b\mathbf{m}^* + c\mathbf{t}. \tag{2.19}$$

The coefficients are determined to yield

$$a + a^* = \frac{1}{2}(\dot{\mathbf{m}}.\mathbf{m}^* + \dot{\mathbf{m}}^*.\mathbf{m}) = \frac{1}{2}\frac{\partial}{\partial t}(\mathbf{m}.\mathbf{m}^*) = 0 \implies a = i\phi(s,t), \tag{2.20}$$

$$b = \frac{1}{2}(\dot{\mathbf{m}}.\mathbf{m}) = \frac{1}{4}\frac{\partial}{\partial t}(\mathbf{m}.\mathbf{m}) = 0, \tag{2.21}$$

$$c = -\mathbf{m}.\dot{\mathbf{t}} = -i\psi_s, \tag{2.22}$$

where $\phi(s,t)$ is some real-valued function.

Thus, $\dot{\mathbf{m}}$ is rewritten as

$$\dot{\mathbf{m}} = i\phi(s,t)\mathbf{m} - i\psi_s\mathbf{t}. \tag{2.23}$$

With the alternative equivalent expression for $\mathbf{m}_s$ as

$$\dot{\mathbf{m}}_s = i\phi_s\mathbf{m} - i\phi\psi\mathbf{t} - \frac{1}{2}i\psi_s(\psi^*\mathbf{m} + \psi\mathbf{m}^*), \tag{2.24}$$

the coefficients of $\mathbf{t}, \mathbf{m}$ and $\mathbf{m}^*$ in Equations (2.18) and (2.24) are equated. Since the $\mathbf{m}^*$ coefficients already match, the $\mathbf{m}$ coefficients are equated to give

$$\phi_s = \frac{1}{2}\frac{\partial}{\partial s}|\psi^2|. \tag{2.25}$$

The real valued function $\phi(s,t)$ is determined as

$$\phi(s,t) = \frac{1}{2}|\psi^2| + A(t), \tag{2.26}$$

where $A(t)$ is an arbitrary function of time, which may without loss of generality be chosen to be zero.

When the $\mathbf{t}$ coefficients are equated, the equation for $\psi(s,t)$ takes the form

$$\dot{\psi} = i\phi\psi + i\psi_{ss}. \tag{2.27}$$

The final evolution equation for $\psi(s,t)$ is then obtained as

$$\dot{\psi} = iA(t)\psi + i\psi_{ss} + \left(\frac{i}{2}\right)|\psi|^2\psi. \tag{2.28}$$

Equation (2.28) is a form of the cubic nonlinear Schrödinger equation (NLS) as obtained by Hasimoto in [1].

2.4 Inverse Map: $\{\kappa(s,t), \tau(s,t)\} \mapsto \{\mathbf{r}(s,t)\}$

Once the curvature $\kappa(s,t)$ and torsion $\tau(s,t)$ have been obtained from $\psi(s,t)$, the solution needs to be mapped back to the position vector $\mathbf{r}(s,t)$ to find the motion of the vortex filament, so that the exact shape of its curve can be obtained. This is done by finding the unit tangential, normal and binormal vectors $\mathbf{t}, \mathbf{n}$ and $\mathbf{b}$ respectively using the Frenet-Serret equations given below

$$\frac{d\mathbf{t}}{ds} = \kappa\mathbf{n}, \tag{2.29}$$

$$\frac{d\mathbf{n}}{ds} = -\kappa\mathbf{t} + \tau\mathbf{b}, \tag{2.30}$$

$$\frac{d\mathbf{b}}{ds} = -\tau\mathbf{n}. \tag{2.31}$$

These three equations can be expressed as an equivalent system of first-order ODEs

$$\frac{d}{ds}\begin{bmatrix}\mathbf{t}\\ \mathbf{n}\\ \mathbf{b}\end{bmatrix} = \begin{bmatrix}0 & \kappa(s,t) & 0\\ -\kappa(s,t) & 0 & \tau(s,t)\\ 0 & -\tau(s,t) & 0\end{bmatrix}\begin{bmatrix}\mathbf{t}\\ \mathbf{n}\\ \mathbf{b}\end{bmatrix}. \tag{2.32}$$

The general procedure then involves solving for $\mathbf{t}, \mathbf{n}$ and $\mathbf{b}$ to obtain $\mathbf{t}$ since

$$\mathbf{t} = \frac{d\mathbf{r}/ds}{|d\mathbf{r}/ds|}, \tag{2.33}$$

from which the complete dimensionalised solution for $\mathbf{r}(s,t) = (x(s,t), y(s,t), z(s,t))$ can be extracted.

For simplicity, this can be represented conveniently as a single first-order ODE in the form

$$\frac{d\mathbf{W}}{ds} = \mathcal{A}(s,t)\mathbf{W}, \tag{2.34}$$

where $\mathbf{W} = \begin{bmatrix}\mathbf{t} & \mathbf{n} & \mathbf{b}\end{bmatrix}^{\mathrm{T}}$ and

$$\mathcal{A}(s,t) = \begin{bmatrix}0 & \kappa(s,t) & 0\\ -\kappa(s,t) & 0 & \tau(s,t)\\ 0 & -\tau(s,t) & 0\end{bmatrix}.$$

The solution of such an equation requires the use of a matrix exponential

$\exp(-\int_0^s \mathcal{A}(\sigma,t)d\sigma)$ as an ansatz for the integrating factor.

Definition 2.1 (Matrix Exponential)**.** A matrix exponential, for an $n \times n$ matrix $\mathcal{B}$, is defined as

$$\exp(\mathcal{B}) = \sum_{k=0}^{\infty} \frac{1}{k!}\mathcal{B}^k. \tag{2.35}$$

If $\mathcal{B}$ is of finite order and well-defined (which holds in the present case), then the series above would converge.

Multiplying both sides of Equation (2.34) by the matrix exponential yields

$$\exp\left(-\int_0^s \mathcal{A}(\sigma,t)d\sigma\right)\left[\frac{d\mathbf{W}}{ds} - \mathcal{A}(s,t)\mathbf{W}\right] = \mathbf{0}, \tag{2.36}$$

so

$$\frac{d}{ds}\left[\exp\left(-\int_0^s \mathcal{A}(\sigma,t)d\sigma\right)\mathbf{W}(s,t)\right] = \mathbf{0}, \tag{2.37}$$

which implies

$$\exp\left(-\int_0^s \mathcal{A}(\sigma,t)d\sigma\right)\mathbf{W}(s,t) = \mathbf{C}(t), \tag{2.38}$$

where $\mathbf{C}(t)$ is a constant matrix in arclength s that may be dependent on time t.

If $\exp(-\int_0^s \mathcal{A}(\sigma,t)d\sigma) = \mathcal{Q}(s,t)$ exists and is non-singular, then $\mathcal{Q}^{-1}(s,t)$ exists and is given by $\mathcal{Q}^{-1}(s,t) = \exp(\int_0^s \mathcal{A}(\sigma,t)d\sigma)$.

On multiplying both sides by $\mathcal{Q}^{-1}(s,t)$, Equation (2.38) becomes

$$\mathbf{W}(s,t) = \exp(\mathcal{M}(s,t))\mathbf{C}(t), \tag{2.39}$$

where

$$\mathcal{M}(s,t) = \begin{bmatrix} 0 & \int_0^s \kappa(\sigma,t)d\sigma & 0 \\ -\int_0^s \kappa(\sigma,t)d\sigma & 0 & \int_0^s \tau(\sigma,t)d\sigma \\ 0 & -\int_0^s \tau(\sigma,t)d\sigma & 0 \end{bmatrix}.$$

In Appendix A, it is shown how to calculate $\mathbf{W}(s,t)$ from (2.39) with the help of an example to demonstrate the method.

A solution, $\mathbf{W}(s,t)$ to Equation (2.39) can be split component-wise to find $\mathbf{r}(s,t)$ as

$$\begin{bmatrix} \mathbf{t}(s,t) \\ \mathbf{n}(s,t) \\ \mathbf{b}(s,t) \end{bmatrix} = \begin{bmatrix} \mathbf{W_1}(s,t) \\ \mathbf{W_2}(s,t) \\ \mathbf{W_3}(s,t) \end{bmatrix}, \tag{2.40}$$

so

$$\mathbf{t}(s,t) = \mathbf{W_1}(s,t), \tag{2.41}$$

which implies

$$\frac{d\mathbf{r}(s,t)/ds}{|d\mathbf{r}(s,t)/ds|} = \mathbf{W_1}(s,t) = (W_{1x}(s,t), W_{1y}(s,t), W_{1z}(s,t))^{\mathrm{T}}. \tag{2.42}$$

Using the form of $\mathbf{r}(s,t) = (x(s,t), y(s,t), z(s,t))$, enables computation of $\frac{d\mathbf{r}}{ds} = (\frac{dx}{ds}, \frac{dy}{ds}, \frac{dz}{ds})$, $|\frac{d\mathbf{r}}{ds}| = \sqrt{\left(\frac{dx}{ds}\right)^2 + \left(\frac{dy}{ds}\right)^2 + \left(\frac{dz}{ds}\right)^2}$ and

$$\frac{1}{\sqrt{\left(\frac{dx}{ds}\right)^2 + \left(\frac{dy}{ds}\right)^2 + \left(\frac{dz}{ds}\right)^2}} \begin{bmatrix} \frac{dx}{ds} \\ \frac{dy}{ds} \\ \frac{dz}{ds} \end{bmatrix} = \begin{bmatrix} W_{1x}(s,t) \\ W_{1y}(s,t) \\ W_{1z}(s,t) \end{bmatrix}. \tag{2.43}$$

Assuming $|\frac{d\mathbf{r}}{ds}| = \sqrt{\left(\frac{dx}{ds}\right)^2 + \left(\frac{dy}{ds}\right)^2 + \left(\frac{dz}{ds}\right)^2} = 1$, the individual components for $\mathbf{r}(s,t)$ can be determined as

$$\frac{dx}{ds} = W_{1x}(s,t), \quad \text{so} \quad x(s,t) = \int_0^s W_{1x}(\sigma,t)d\sigma + x_0(t), \tag{2.44}$$

$$\frac{dy}{ds} = W_{1y}(s,t), \quad \text{so} \quad y(s,t) = \int_0^s W_{1y}(\sigma,t)d\sigma + y_0(t), \tag{2.45}$$

$$\frac{dz}{ds} = W_{1z}(s,t), \quad \text{so} \quad z(s,t) = \int_0^s W_{1z}(\sigma,t)d\sigma + z_0(t). \tag{2.46}$$

It is worth stating that an essential condition for the final expression for $\mathbf{r}(s,t)$ given below in Equation (2.47) to hold is that $W_{1x}^2 + W_{1y}^2 + W_{1z}^2 = 1$. If this holds, then

$$\mathbf{r}(s,t) = \begin{bmatrix} \int_0^s W_{1x}(\sigma,t)d\sigma + x_0(t) \\ \int_0^s W_{1y}(\sigma,t)d\sigma + y_0(t) \\ \int_0^s W_{1z}(\sigma,t)d\sigma + z_0(t) \end{bmatrix}. \tag{2.47}$$

Determination of $\mathbf{r}(s,t)$ in this manner enables an exact plot of the vortex filament curve to be constructed in the Cartesian (x,y,z) space. For further details, the reader is directed to refer to Appendix A.

2.5 Peregrine Soliton on a Classical Vortex Filament

To obtain the classical solution of a Peregrine soliton on a vortex filament, the function $\hat{\psi}(\hat{s},\hat{t})$ from [5] is used and this is given below as

$$\hat{\psi}(\hat{s},\hat{t}) = \sqrt{|\omega|}\Big(1 - \frac{4(1+2|\omega|i\hat{t})}{1+4[|\omega|\hat{s}^2+\omega^2\hat{t}^2]}\Big)\mathrm{e}^{-i\omega\hat{t}}, \tag{2.48}$$

where $\omega < 0$ is a spectral parameter to indicate that a family of such rational solitons exist as solutions to the cubic NLS

$$i\dot{\hat{\psi}} + \frac{1}{2}\hat{\psi}_{\hat{s}\hat{s}} + |\hat{\psi}|^2\hat{\psi} = 0, \tag{2.49}$$

where $\dot{\hat{\psi}} = \frac{d}{d\hat{t}}\hat{\psi}(\hat{\hat{s}},\hat{t})$.

In order to scale the NLS of the Peregrine soliton in Equation (2.49) appropriately to match the form of the NLS for the vortex filament as given in Equation (1.2) in Chapter 1 (which will be employed throughout the analysis to follow), a coordinate transformation $s = a\hat{s}, \psi = b\hat{\psi}, t = c\hat{t}$ is introduced to map the Peregrine soliton NLS

$$i\dot{\hat{\psi}} + \frac{1}{2}\hat{\psi}_{\hat{s}\hat{s}} + |\hat{\psi}|^2\hat{\psi} = 0, \tag{2.50}$$

to the vortex filament NLS

$$i\dot{\psi} + \psi_{ss} + \frac{1}{2}|\psi|^2\psi = 0. \tag{2.51}$$

Substitution then yields

$$i\,c\,b\,\dot{\hat{\psi}} + a^2 b\,\hat{\psi}_{\hat{s}\hat{s}} + \frac{1}{2}b^3\,|\hat{\psi}|^2\hat{\psi} = 0, \tag{2.52}$$

so that

$$i\,\dot{\hat{\psi}} + \frac{a^2}{c}\,\hat{\psi}_{\hat{s}\hat{s}} + \frac{1}{2}\frac{b^2}{c}\,|\hat{\psi}|^2\hat{\psi} = 0, \tag{2.53}$$

which when compared to Equation (2.49) implies,

$$\frac{a^2}{c} = \frac{1}{2}, \quad \frac{1}{2}\frac{b^2}{c} = 1. \tag{2.54}$$

Thus,

$$a = \frac{1}{\sqrt{2}}, \quad b = \sqrt{2}, \quad c = 1. \tag{2.55}$$

This results in the transformed set of coordinates

$$s = \frac{\hat{s}}{\sqrt{2}}, \quad \psi = \sqrt{2}\hat{\psi}, \quad t = \hat{t}. \tag{2.56}$$

The NLS solution $\psi(s,t)$ for the vortex filament can then be written as

$$\psi(s,t) = \sqrt{2}\hat{\psi}(\hat{s},t) = \sqrt{2}\hat{\psi}(\sqrt{2}s,t) = \sqrt{2|\omega|}\Big(1 - \frac{4(1+2|\omega|it)}{1+4[2|\omega|s^2+\omega^2t^2]}\Big)\mathrm{e}^{-i\omega t}. \tag{2.57}$$

Since this expression for $\psi(s,t)$ is not explicitly split into its real and imaginary components $R(s,t)$ and $I(s,t)$ respectively, a transformation from its polar representation

$$\psi(s,t) = \kappa(s,t)\exp(i\int_0^s \tau(\sigma,t)d\sigma), \tag{2.58}$$

to its Cartesian form

$$\psi(s,t) = R(s,t) + iI(s,t), \tag{2.59}$$

is required. This results in the following expressions for curvature $\kappa(s,t)$ and torsion $\tau(s,t)$ in terms of $R(s,t)$ and $I(s,t)$

$$\kappa(s,t) = \sqrt{R^2(s,t) + I^2(s,t)}, \tag{2.60}$$

$$\tau(s,t) = \frac{d}{ds}\Big\{\tan^{-1}\Big(\frac{I(s,t)}{R(s,t)}\Big)\Big\}. \tag{2.61}$$

$\psi(s,t)$ can be rewritten in Cartesian form as

$$\psi(s,t) = \sqrt{2|\omega|}\Big\{\Big(1 - \frac{4}{1+4(2|\omega|s^2+\omega^2t^2)}\Big) - i\Big(\frac{8|\omega|t}{1+4(2|\omega|s^2+\omega^2t^2)}\Big)\Big\} \times (\cos\omega t - i\sin\omega t). \tag{2.62}$$

It is then useful to denote

$$f(s,t) = \left(1 - \frac{4}{1+4(2|\omega|s^2+\omega^2t^2)}\right), \tag{2.63}$$

and

$$g(s,t) = \left(\frac{8|\omega|t}{1+4(2|\omega|s^2+\omega^2t^2)}\right). \tag{2.64}$$

Then,

$$\psi(s,t) = \sqrt{2|\omega|}[(f\cos\omega t - g\sin\omega t) + i(-f\sin\omega t - g\cos\omega t)], \tag{2.65}$$

so that

$$R(s,t) = \sqrt{2|\omega|}[f\cos\omega t - g\sin\omega t], \tag{2.66}$$

and

$$I(s,t) = -\sqrt{2|\omega|}[f\sin\omega t + g\cos\omega t]. \tag{2.67}$$

The final classical solution for the curvature $\kappa(s,t)$ for a Peregrine soliton after re-substituting for the expressions of f and g, takes the form

$$\kappa(s,t) = \sqrt{2|\omega|}\sqrt{\Big(1 - \frac{4}{1+4(2|\omega|s^2+\omega^2t^2)}\Big)^2 + \Big(\frac{8|\omega|t}{1+4(2|\omega|s^2+\omega^2t^2)}\Big)^2}. \tag{2.68}$$

The torsion $\tau(s,t)$ is then determined using

$$\tau(s,t) = \frac{d}{ds}\Big[\tan^{-1}\Big(-\frac{f\sin\omega t + g\cos\omega t}{f\cos\omega t - g\sin\omega t}\Big)\Big]. \tag{2.69}$$

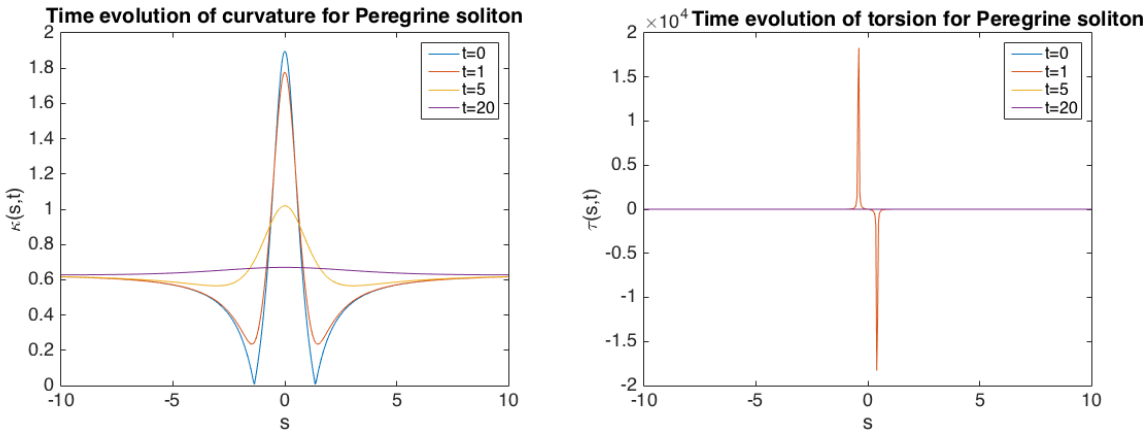

(a) (b)

Figure 2.3: (a): Time evolution of curvature for classical Peregrine soliton; (b): Time evolution of torsion for classical Peregrine soliton ($\omega = -0.2$).

This simplifies to

$$\tau(s,t) = \frac{f'g - gf'}{f^2 + g^2}, \tag{2.70}$$

where $()' = \frac{d}{ds}()$, so the final classical solution for the torsion $\tau(s,t)$ for a Peregrine soliton after re-substituting for the expressions of f, f', g and g', takes the form

$$\tau(s,t) = \frac{64|\omega|st\left[|\omega| + \frac{4(|\omega|-1)}{1+4(2|\omega|s^2+\omega^2t^2)}\right]}{(64\omega^2t^2 + 4(2|\omega|s^2 + \omega^2t^2) - 3)^2}. \tag{2.71}$$

Figures 2.3(a) and 2.3(b) highlight the variation of both curvature and torsion with time for the classical Peregrine soliton solution and it can be observed that both the solutions vary spatio-temporally. The curvature plot demonstrates the characteristic peak amplitude bump at the origin $s = 0$ as it flattens out symmetrically to a constant value at either end of the vortex filament as $s \to \infty$. Moreover, as time progresses, the amplitude decreases from its maximum value at $t = 0$ with the bump tending to its constant straight-line value as $t \to \infty$. It also aptly matches the plot in Figure 1.2 in Chapter 1 from [5].

The torsion curve, on the other hand reaches its peak amplitude in the form of sharp spikes for smaller time values with $\tau \to 0$ as $t \to \infty$. The location of these spikes can be determined by setting the denominator in the torsion expression (2.71) to zero.

There are thus two singular points at

$$s_1 = \sqrt{\frac{3 - 68\omega^2 t^2}{8|\omega|}}, \quad s_2 = -\sqrt{\frac{3 - 68\omega^2 t^2}{8|\omega|}}, \tag{2.72}$$

provided $3 - 68\omega^2 t^2 > 0$; implying that $t < \sqrt{\frac{3}{68\omega^2}}$. So, for $0 < t < \sqrt{\frac{3}{68}}\frac{1}{|\omega|}$, there are two singular points, which depend on time, for the torsion τ. When $t = \sqrt{\frac{3}{68}}\frac{1}{|\omega|}$, then there is one singular point at $s = 0$. Finally, for larger time, namely $t > \sqrt{\frac{3}{68}}\frac{1}{|\omega|}$, there are no singular points. Hence, for longer time, the solution becomes more smooth.

A point worth mentioning is the time symmetry/asymmetry for the curvature and torsion respectively that is, $\kappa(s,t) = \kappa(s,-t)$ and $\kappa(s,t) = \kappa(-s,t)$, so the curvature is symmetric in both space and time (even function in t and s). On the other hand, $\tau(s,t) = -\tau(s,-t)$ and $\tau(s,t) = -\tau(-s,t)$, so the torsion is rotationally symmetric in both space and time (odd function in t and s) about the origin $s = 0$. Thus, without loss of generality, plots for $t \geq 0$ are sufficient to obtain information for all behaviours.

2.6 Akhmediev Breather on a Classical Vortex Filament

To obtain the classical solution of a spatially-periodic Akhmediev breather on a vortex filament, the function $\psi(s,t)$ from [26] is used and this is given below as

$$\psi(s,t) = \bar{\kappa_0} \mathrm{e}^{i\left(\frac{\bar{\kappa_0}^2 t}{2} + \bar{\tau_0} s + \left(\bar{\kappa_0}^2 - \bar{\tau_0}^2\right)t\right)} \frac{\cosh(\Omega \bar{\kappa_0}^2 t/4 - 2i\phi) - \cos(\phi)\cos(k\bar{\kappa_0}s/2 - k\bar{\tau_0}\bar{\kappa_0}t)}{\cosh(\Omega \bar{\kappa_0}^2 t/4) - \cos(\phi)\cos(k\bar{\kappa_0}s/2 - k\bar{\tau_0}\bar{\kappa_0}t)}, \tag{2.73}$$

where, $k = 2\sin(\phi)$ and $\Omega = 2\sin(2\phi)$. In this expression, ϕ is a real variable, while $\bar{\kappa_0}$ and $\bar{\tau_0}$ are constants corresponding to the curvature and torsion respectively for the unperturbed helical vortex filament. This complex function $\psi(s,t)$ is a solution of the cubic NLS equation

$$i\dot{\psi} + \psi_{ss} + \frac{1}{2}|\psi|^2\psi = 0. \tag{2.74}$$

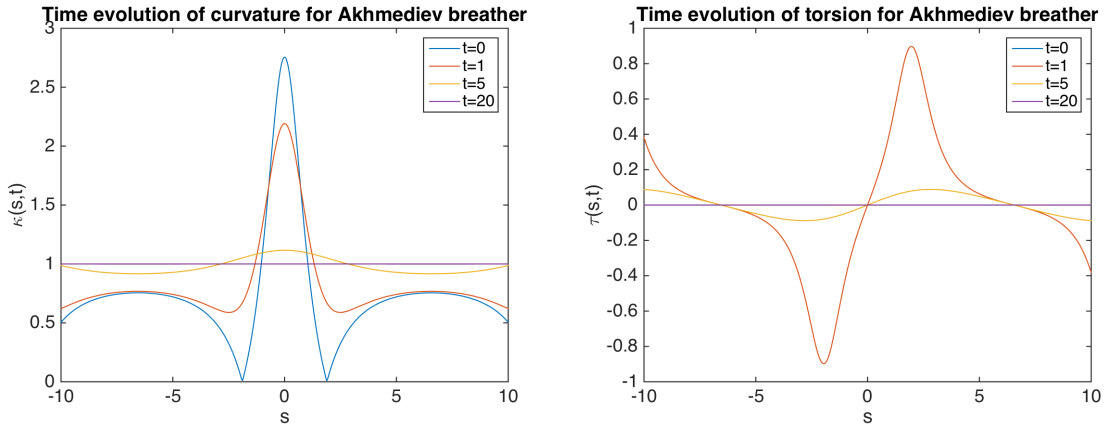

(a) (b)

Figure 2.4: (a): Time evolution of curvature for classical Akhmediev breather; (b): Time evolution of torsion for classical Akhmediev breather ($\bar{\kappa_0} = 1, \bar{\tau_0} = 0$ and $\phi = 0.5$).

It is worth noting that the $\psi(s,t)$ function for the general Akhmediev breather reduces to the special limiting case of the Peregrine soliton described in Section 2.5 as $\phi \to 0$ or as the spatial period approaches ∞. Writing (2.73) in the required form and carrying out computations similar to Section 2.5, it is found that the curvature $\kappa(s,t)$ and torsion $\tau(s,t)$ are given by

$$\kappa(s,t) = \frac{\bar{\kappa_0}\sqrt{\left(\cos^2\phi\cos^2\xi - 2\cos\phi\cos 2\phi\cos\xi\cosh\lambda + \cos^2 2\phi\cosh^2\lambda + \sin^2 2\phi\sinh^2\lambda\right)}}{\cosh\lambda - \cos\phi\cos\xi}, \tag{2.75}$$

and

$$\begin{aligned}\tau(s,t) = \Big(&\bar{\tau_0}\cos^2\phi\cos^2\xi - 2\bar{\tau_0}\cos\phi\cos 2\phi\cos\xi\cosh\lambda + \bar{\tau_0}\cos^2 2\phi\cosh^2\lambda \\ &+ \bar{\kappa_0}\cos\phi\sin\phi\sin 2\phi\sin\xi\sinh\lambda + \bar{\tau_0}\sin^2 2\phi\sinh^2\lambda\Big)/ \\ &\Big(\cos^2\phi\cos^2\xi - 2\cos\phi\cos 2\phi\cos\xi\cosh\lambda + \cos^2 2\phi\cosh^2\lambda + \sin^2 2\phi\sinh^2\lambda\Big),\end{aligned} \tag{2.76}$$

where, $\xi = \bar{\kappa_0}(s - 2\bar{\tau_0}\,t)\sin\phi$, $\eta = \bar{\tau_0}s + 3/2\bar{\kappa_0}^2\,t - \bar{\tau_0}^2\,t$, $\lambda = \bar{\kappa_0}^2 t\cos\phi\sin\phi$.

Figures 2.4(a) and 2.4(b) highlight the variation of both curvature and torsion with time for the classical Akhmediev breather solution and it can be observed that both the solutions vary spatio-temporally. The curvature plot demonstrates the

characteristic peak amplitude bump at the origin $s = 0$ as it flattens out symmetrically to a constant value at either end of the vortex filament as $s \to \infty$. Moreover, as time progresses, the amplitude decreases from its maximum value at $t = 0$ with the bump tending to its constant straight-line value as $t \to \infty$. The curvature plot is rather similar to its Peregrine soliton analogue, except for the peak amplitude bump, which in this case, is wider on either side of $s = 0$. It also aptly matches the figure obtained by Dysthe and Trulsen in [26].

For the case shown in Figure 2.4(b) when $\bar{\kappa_0} = 1, \bar{\tau_0} = 0$ and $\phi = 0.5$, the two peaks with the maximum torsion value can be computed by setting the derivative of the torsion expression in (2.76) to zero after substituting the constant values mentioned. This indicates that the maximum torsion values occur at the two points, $s = -1.96$ and $s = 1.96$ for $t = 1$. For larger times such as $t = 20$, there are no singular points and so the solution becomes more smooth. For very large times, the vortex filament should take the form of a line filament.

A point worth mentioning is the time symmetry/asymmetry for the curvature and torsion respectively, for the special case when $\bar{\tau_0} = 0$ as evident from Figures 2.4(a) and 2.4(b) that is, $\kappa(s,t) = \kappa(s,-t)$ and $\kappa(s,t) = \kappa(-s,t)$, so the curvature is symmetric in both space and time (even function in t and s). On the other hand, $\tau(s,t) = -\tau(s,-t)$ and $\tau(s,t) = -\tau(-s,t)$, so the torsion is rotationally symmetric in both space and time (odd function in t and s) about the origin $s = 0$ when $\bar{\tau_0} = 0$.

Chapter 3

Quantum Hasimoto Map ($\mathbf{U} = \mathbf{0}$)

3.1 Hasimoto Map: $\{\mathbf{r}(s,t)\} \mapsto \{\kappa(s,t), \tau(s,t)\}$

The mathematical formulation for the generalised quantum analogue for the Hasimoto map is reproduced entirely from [2] in this section as the fundamental tool used to obtain solutions to the quantum LIA equation

$$\mathbf{v} = \kappa\,\mathbf{t} \times \mathbf{n} + \alpha\,\mathbf{t} \times (\mathbf{U} - \kappa\,\mathbf{t} \times \mathbf{n}) - \alpha'\,\mathbf{t} \times (\mathbf{t} \times (\mathbf{U} - \kappa\,\mathbf{t} \times \mathbf{n})). \tag{3.1}$$

On differentiating with respect to the arclength s and using $|\mathbf{t}| = 1$ since $\mathbf{t}$ is the unit tangential vector, Equation (3.1) transforms to a vector conservation law of the form

$$\dot{\mathbf{t}} = \frac{\partial}{\partial s}\{(1-\alpha')\mathbf{t} \times \mathbf{t}_s + \alpha\mathbf{t}_s + \alpha\mathbf{t} \times \mathbf{U} - \alpha'(\mathbf{t} \cdot \mathbf{U})\mathbf{t}\}. \tag{3.2}$$

A crucial assumption made in the derivation of the quantum Hasimoto transformation is that $\mathbf{U}$ is sufficiently small with $\mathbf{U} = O(\alpha)$ so that $\alpha\mathbf{U} = O(\alpha^2)$, which can be neglected by setting $\mathbf{U} = \mathbf{0}$. The Frenet-Serret formulae $\mathbf{t}_s = \kappa\mathbf{n}$, $\mathbf{n}_s = -\kappa\mathbf{t} + \tau\mathbf{b}$ and $\mathbf{b}_s = -\tau\mathbf{n}$ are then used to yield

$$\dot{\mathbf{t}} = (1-\alpha')(\kappa\mathbf{b})_s + \alpha\mathbf{t}_{ss}. \tag{3.3}$$

The complex variable $\psi(s,t)$ is defined in a similar manner as given in Section 2.3 in Chapter 2 where

$$\psi(s,t) = \kappa(s,t)\,\mathrm{e}^{i\int_0^s \tau(\hat{s},t)\mathrm{d}\hat{s}}, \tag{3.4}$$

with $\kappa(s,t)$ and $\tau(s,t)$ representing curvature and torsion respectively.

Following the method of Section 2.3, the evolution equation for $\psi(s,t)$ is then obtained in [2] as

$$\dot{\psi} = iA(t)\psi + (i(1-\alpha') + \alpha)\psi_{ss} + \left(\frac{(1-\alpha')\,i}{2} - \alpha\right)|\psi^2|\psi \\ - \frac{\alpha}{2}\psi\int_0^s \{\psi(\hat{s},t)\psi_s(\hat{s},t)^* - \psi(\hat{s},t)^*\psi_s(\hat{s},t)d\hat{s}\}. \tag{3.5}$$

Equation (3.5), obtained from the quantum Hasimoto formulation, is the complex Ginsburg-Landau equation (GLE) with an extra dissipation term, which for classical fluids (when $\alpha, \alpha' = 0$) reduces to the cubic nonlinear Schrödinger equation (NLS) [1].

A concluding remark to make is that the arbitrary function $A(t)$ is generally chosen to satisfy structural conditions that the vortex filament must adhere to and this usually varies depending on the type of wave solution sought.

3.2 Perturbation of Quantum Hasimoto Map Solutions

To obtain the quantum solution $\psi(s,t)$ for a rogue wave on a vortex filament, the classical solution is denoted by $\psi_0(s,t)$, whose exact form would be specific to the solution being sought.

Taking $A(t) \equiv 0$ in the GLE in Equation (3.5) in Section 3.1, scaling the time variable $t \mapsto (1-\alpha')t$, and defining the parameter $\epsilon = \frac{\alpha}{1-\alpha'} \ll 1$, Equation (3.5) can be rewritten as

$$\dot{\psi} = (i+\epsilon)\psi_{ss} + \left(\frac{i}{2} - \epsilon\right)|\psi|^2\psi - \frac{\epsilon}{2}\psi\int_0^s \{\psi\psi_s^* - \psi^*\psi_s d\tilde{s}\}. \tag{3.6}$$

A perturbation expansion for $\psi(s,t)$ is assumed as

$$\psi(s,t) = \psi_0(s,t) + \epsilon\psi_1(s,t) + O(\epsilon^2), \tag{3.7}$$

where only terms up to first-order are considered, since second and higher-order terms are very small ($\epsilon \ll 1$).

Substitution of the expression (3.7) in Equation (3.6) and dividing by i, gives

$$\begin{aligned} &i\dot{\psi_0} + \psi_{0ss} + \frac{1}{2}|\psi_0|^2\psi_0 \\ &\quad + \epsilon\Big\{i\dot{\psi_1} + \psi_{1ss} - i\psi_{0ss} + \Big(\frac{\psi_0^2\psi_1^* + 2|\psi_0|^2\psi_1}{2}\Big) \\ &\quad + i|\psi_0|^2\psi_0 + \frac{i}{2}\int_0^s(\psi_0\psi_{0s}^* - {\psi_0}^*\psi_{0s})d\tilde{s}\Big\} + O(\epsilon^2) = 0. \end{aligned} \tag{3.8}$$

Equating both the zeroth and first-order terms in Equation (3.8) yield

$$O(1): \quad i\dot{\psi_0} + \psi_{0ss} + \frac{1}{2}|\psi_0|^2\psi_0 = 0, \tag{3.9}$$

$$\begin{aligned} O(\epsilon): \quad &i\dot{\psi_1} + \psi_{1ss} + \frac{1}{2}\psi_0^2\psi_1^* + |\psi_0^2|\psi_1 \\ &= i\left\{\psi_{0ss} - |\psi_0|^2\psi_0 - \frac{\psi_0}{2}\int_0^s\{\psi_0\psi_{0s}^* - \psi_0^*\psi_{0s}\}d\tilde{s}\right\}. \end{aligned} \tag{3.10}$$

The $O(1)$ equation will always be satisfied with the choice of solution given by the classical solution denoted by $\psi_0(s,t)$. Solving the $O(\epsilon)$ equation for $\psi_1(s,t)$ will lead to expressions for curvature and torsion for the quantum case. This was done in [2] for the one-soliton solution in the quantum case.

Writing and substituting $\psi_0(s,t) = R(s,t) + iI(s,t)$ in terms of its real and imaginary components in Equation (3.10) yields

$$\begin{aligned} &i\dot{\psi_1} + \psi_{1ss} + \frac{1}{2}(R^2 - I^2 + 2iRI)\psi_1^* + (R^2 + I^2)\psi_1 \\ &\quad = i\Big\{R_{ss} + iI_{ss} - (R^2 + I^2)(R + iI) - \frac{(R + iI)}{2}\int_0^s(R + iI)(R_s - iI_s) \\ &\qquad - (R - iI)(R_s + iI_s)\,d\tilde{s}\Big\} \\ &\quad = iR_{ss} - I_{ss} - i(R^2 + I^2)R + (R^2 + I^2)I - \frac{i(R + iI)}{2}\int_0^s 2i(IR_s - RI_s)\,d\tilde{s} \\ &\quad = -I_{ss} + (R^2 + I^2)I + R\int_0^s(IR_s - RI_s)\,d\tilde{s} \\ &\qquad + i\left\{R_{ss} - (R^2 + I^2)R + I\int_0^s(IR_s - RI_s)\,d\tilde{s}\right\}. \end{aligned} \tag{3.11}$$

Unfortunately, while this equation is linear in (3.11), it has coefficients which depend on s and t in the case of breathers and the Peregrine soliton. For these cases, it was not possible to solve (3.11) for $\psi_1(s,t)$, or to even accurately approximate a solution,

since some of the coefficients became singular. This necessitated the need to seek out a different approach

3.3 Motivation for a New Model of Quantum Vortex Filaments

The complicated expressions obtained in Equation (3.11) for the perturbed rogue waves on quantum vortex filaments using the $\mathbf{U} = \mathbf{0}$ model made it rather difficult to yield both analytical solutions and numerical plots for the Peregrine soliton and Akhmediev breather. This can be primarily attributed to the large number of multi-dimensional integrals present in the formulas, making evaluation of the expressions extremely tedious and complex. Introducing simplifying assumptions in the calculation of every term tended to reduce the accuracy of the solutions, which in turn significantly altered the behaviour of the solutions, beyond what was expected. Thus, it was decided that in order to obtain satisfactory solutions for the quantum case, a new model needed to be formulated that would rely on a perturbation of an entirely different map, as opposed to the Hasimoto map that had been employed so far. This motivated the development of the $\mathbf{U} \neq \mathbf{0}$ model presented in Chapter 4, that generalises the model even further by accounting for both mutual friction and normal fluid velocity effects, with the latter having been neglected earlier.

Chapter 4

Quantum Model ($\mathbf{U} \neq \mathbf{0}$)

4.1 Map for $\mathbf{U} \neq \mathbf{0}$: $\{\mathbf{r}(s,t)\} \mapsto \{v(s,t)\}$

To account for the case of non-negligible normal fluid velocity when $\mathbf{U} \neq \mathbf{0}$, the vector conservation law with the unit tangential vector $|\mathbf{t}| = 1$, is similar to Equation (3.2) in Chapter 3 and takes the form

$$\dot{\mathbf{t}} = \frac{\partial}{\partial s}\{(1-\alpha')\mathbf{t} \times \mathbf{t}_s + \alpha \mathbf{t}_s + \alpha \mathbf{t} \times \mathbf{U} - \alpha'(\mathbf{t} \cdot \mathbf{U})\mathbf{t}\}. \tag{4.1}$$

Due to the appearance of $\mathbf{U}$ in the equation, it is not possible to find any equation for $\psi(s,t) = \kappa(s,t)\, \mathrm{e}^{i\int_0^s \tau(\hat{s},t)\mathrm{d}\hat{s}}$, so the problem needs to be approached differently.

By introducing a complex variable function $v(s,t), v : \mathbb{R}^2 \mapsto \mathbb{C}$, the three components of the unit tangential vector $\mathbf{t}$ can be written as

$$\mathbf{t} = \left(\frac{v+v^*}{2}, \frac{v-v^*}{2i}, \sqrt{1-|v^2|}\right). \tag{4.2}$$

It is worth noting that both $\frac{v+v^*}{2} = \mathrm{Re}(v)$ and $\frac{v-v^*}{2i} = \mathrm{Im}(v)$ are real-valued and hence $\mathbf{t}$ is written as a vector with real components.

Moreover,

$$\begin{aligned}|\mathbf{t}|^2 &= \left(\frac{v+v^*}{2}\right)^2 + \left(\frac{v-v^*}{2i}\right)^2 + \left(\sqrt{1-|v^2|}\right)^2 \\ &= \frac{1}{4}(v^2+2vv^*+v^{*2}) - \frac{1}{4}(v^2-2vv^*+v^{*2}) + 1 - |v|^2 \\ &= vv^* + 1 - |v|^2 = |v|^2 + 1 - |v|^2 = 1, \end{aligned} \tag{4.3}$$

hence $|\mathbf{t}| = 1$, implying that the form of $\mathbf{t}$, as written above, is a unit vector.

This special form for $\mathbf{t}$, when substituted into Equation (4.1), yields

$$\frac{\partial}{\partial t}\left(\frac{v+v^*}{2}\right) = \mathrm{rhs}_1[v, v^*], \tag{4.4}$$

$$\frac{\partial}{\partial t}\left(\frac{v-v^*}{2i}\right) = \mathrm{rhs}_2[v, v^*], \tag{4.5}$$

$$\frac{\partial}{\partial t}\left(\sqrt{1-|v^2|}\right) = \mathrm{rhs}_3[v, v^*], \tag{4.6}$$

where $\mathrm{rhs}_k[v, v^*]$ is a complicated function of v, v^* and their derivatives in s for $k = 1, 2, 3$ and is given by

$$\begin{aligned}\mathrm{rhs}_1[v, v^*] = \frac{\partial}{\partial s}\Bigg\{ &-(1-\alpha')\left[\frac{|v||v|_s(v-v^*)}{2\sqrt{1-|v^2|}} + \frac{\left(\sqrt{1-|v^2|}\right)(v_s - v_s^*)}{2}\right] \\ &+ \frac{\alpha(v_s+v_s^*)}{2} + \alpha\left[\left(\frac{v-v^*}{2}\right)U_3 - \left(\sqrt{1-|v^2|}\right)U_2\right] \\ &- \alpha'\Big[\left(\frac{v+v^*}{2}\right)U_1 + \left(\frac{v-v^*}{2}\right)U_2 \\ &+ \left(\sqrt{1-|v^2|}\right)U_3\Big]\left(\frac{v+v^*}{2}\right)\Bigg\}, \end{aligned} \tag{4.7}$$

$$\begin{aligned}\mathrm{rhs}_2[v, v^*] = \frac{\partial}{\partial s}\Bigg\{ &(1-\alpha')\left[\frac{|v||v|_s(v+v^*)}{2\sqrt{1-|v^2|}} + \frac{\left(\sqrt{1-|v^2|}\right)(v_s + v_s^*)}{2}\right] \\ &+ \frac{\alpha(v_s-v_s^*)}{2} + \alpha\left[-\left(\frac{v+v^*}{2}\right)U_3 + \left(\sqrt{1-|v^2|}\right)U_1\right] \\ &- \alpha'\Bigg[\left(\frac{v+v^*}{2}\right)U_1 + \left(\frac{v-v^*}{2}\right)U_2 \\ &+ \left(\sqrt{1-|v^2|}\right)U_3\Bigg]\left(\frac{v-v^*}{2}\right)\Bigg\}, \end{aligned} \tag{4.8}$$

$$\begin{aligned}\mathrm{rhs}_3[v,v^*] = \frac{\partial}{\partial s}\Bigg\{&(1-\alpha')\left[\frac{(v^*v_s - vv_s^*)}{2}\right] - \frac{\alpha|v||v|_s)}{\sqrt{1-|v^2|}} \\ &+\alpha\left[\left(\frac{v+v^*}{2}\right)U_2 - \left(\frac{v-v^*}{2}\right)U_1\right] - \alpha'\Big[\left(\frac{v+v^*}{2}\right)U_1 \\ &+\left(\frac{v-v^*}{2}\right)U_2 + \left(\sqrt{1-|v^2|}\right)U_3\Big]\left(\sqrt{1-|v^2|}\right)\Bigg\}. \end{aligned} \tag{4.9}$$

Since the first two equations are related through complex conjugations, adding the first equation to i times the second, gives

$$\frac{\partial}{\partial t}\Big(\frac{v+v^*}{2}\Big) + i\frac{\partial}{\partial t}\Big(\frac{v-v^*}{2i}\Big) = \mathrm{rhs}_1[v,v^*] + i\,\mathrm{rhs}_2[v,v^*]. \tag{4.10}$$

Yet since,

$$\frac{\partial}{\partial t}\Big(\frac{v+v^*}{2}\Big) + i\frac{\partial}{\partial t}\Big(\frac{v-v^*}{2i}\Big) = \frac{\partial}{\partial t}\Big(\frac{2v}{2}\Big) = \frac{\partial v}{\partial t} = \dot{v}, \tag{4.11}$$

this leads to

$$\begin{aligned}\dot{v} &= \mathrm{rhs}_1[v,v^*] + i\,\mathrm{rhs}_2[v,v^*] \\ &= \frac{\partial}{\partial s}\Bigg\{i(1-\alpha')\frac{v_s}{\sqrt{1-|v|^2}} + \alpha v_s + \frac{i(1-\alpha')(v^2v_s^* - |v|^2v_s)}{2\sqrt{1-|v|^2}} \\ &\quad + \frac{\alpha' U_3|v|^2 v}{\sqrt{1-|v|^2}} - \frac{\alpha' U_3 v}{\sqrt{1-|v|^2}} - i\alpha U_3 v - (U_1+iU_2)\left[\frac{\alpha'}{2}|v|^2 - \frac{i\alpha}{\sqrt{1-|v|^2}}\right] \\ &\quad + \frac{\alpha'}{2}(iU_2 - U_1)v^2\Bigg\}, \end{aligned} \tag{4.12}$$

where $\mathbf{U} = (U_1, U_2, U_3)$.

It is then assumed that the solution is oriented with the tangent vector $\mathbf{t}$, so that the coordinate frame is (y, z, x) for simplicity. It is also assumed that the filament is aligned along the x-axis. As shown by Shivamoggi in [27], the normal fluid flow along the y or z-axis will not have much qualitative influence on the shape of the filament. Hence, it was decided to set $U_1 = 0$ and $U_2 = 0$.

After simplifications, Equation (4.12) gives

$$\dot{v} = \frac{\partial}{\partial s}\left\{ \frac{i(1-\alpha')}{\sqrt{1-|v|^2}} \left[v_s + \frac{v^2 v_s^* - |v|^2 v_s}{2} \right] + \alpha v_s - \alpha' U_3(\sqrt{1-|v|^2})v - i\,\alpha U_3\, v \right\}. \tag{4.13}$$

Yet, it can be seen that

$$\begin{aligned} v_s + \frac{v^2 v_s^* - |v|^2 v_s}{2} &= v_s - |v|^2 v_s + \frac{v^2 v_s^* - |v|^2 v_s}{2} \\ &= (1-|v|^2)v_s + \frac{1}{2} v \frac{\partial}{\partial s}(v v^*) \\ &= (1-|v|^2)v_s + \frac{1}{2} v \frac{\partial}{\partial s}(|v|^2) \\ &= (1-|v|^2)^{3/2} \frac{\partial}{\partial s}\left(\frac{v}{\sqrt{1-|v|^2}} \right). \end{aligned} \tag{4.14}$$

Hence, the final PDE for a vortex filament when $\mathbf{U} \neq \mathbf{0}$ is given by

$$\dot{v} = \frac{\partial}{\partial s}\left[i(1-\alpha')(1-|v|^2) \frac{\partial}{\partial s}\left(\frac{v}{\sqrt{1-|v|^2}} \right) + \alpha v_s - U_3 \left(\alpha' \sqrt{1-|v|^2} + i\alpha \right) v \right]. \tag{4.15}$$

This equation is not similar to the GLE equation (3.5) obtained earlier in Section 3.1 for $\mathbf{U} = \mathbf{0}$. The equation therefore, is expected to be far more complicated to solve.

4.2 Inverse Map for $\mathbf{U} \neq \mathbf{0}$: $\{v(s,t)\} \mapsto \{\mathbf{r}(s,t)\}$

Once $v(s,t)$ has been obtained, the unit tangential vector $\mathbf{t}(s,t)$ can be obtained from Equation (4.2).

Similar to what was done in Section 2.4, the position vector $\mathbf{r}(s,t)$ can be found from

$$x(s,t) = \int_0^s \sqrt{1-|v(\sigma,t)|^2}\, d\sigma + x_0(t), \tag{4.16}$$

$$y(s,t) = \int_0^s \mathrm{Re}(v(\sigma,t))\, d\sigma + y_0(t), \tag{4.17}$$

$$z(s,t) = \int_0^s \mathrm{Im}(v(\sigma,t))\, d\sigma + z_0(t). \tag{4.18}$$

Thus, moving back from the (y, z, x) frame to the (x, y, z) frame gives

$$\mathbf{r}(s,t) = \begin{bmatrix} \int_0^s \sqrt{1-|v(\sigma,t)|^2}d\sigma + x_0(t) \\ \int_0^s \mathrm{Re}(v(\sigma,t))d\sigma + y_0(t) \\ \int_0^s \mathrm{Im}(v(\sigma,t))d\sigma + z_0(t) \end{bmatrix}. \tag{4.19}$$

Using this, the position of any such filament subject to $\mathbf{U} \neq \mathbf{0}$ may be plotted. A remark worth making is that the condition $\frac{\partial}{\partial t}(\sqrt{1-|v|^2}) = \mathrm{rhs}_3[v, v^*]$ was not used. This can be treated as a consistency condition and should be satisfied by any unit vector solution $\mathbf{t}$.

4.3 Perturbation of $\mathbf{U} \neq \mathbf{0}$ Map

It has been shown in the literature sources by Van Gorder [28, 29] that $\alpha' < \alpha \leq 1$ and that α' does not strongly influence the qualitative behaviour of solutions. Therefore, the α' terms can be dropped to reduce the PDE in Equation (4.15) to

$$\dot{v} = i\frac{\partial}{\partial s}\left\{\left(1-|v|^2\right)\frac{\partial}{\partial s}\left(\frac{v}{\sqrt{1-|v|^2}}\right)\right\} + \alpha v_{ss} - i\alpha U_3 v_s. \tag{4.20}$$

The time evolution for v therefore involves three qualitatively distinct terms. The first term in (4.20) is the standard LIA in the classical limit $\alpha \to 0$. Therefore, under the formulation of Section 4.1, the classical LIA is exactly

$$\dot{v} = i\frac{\partial}{\partial s}\left\{\left(1-|v|^2\right)\frac{\partial}{\partial s}\left(\frac{v}{\sqrt{1-|v|^2}}\right)\right\}. \tag{4.21}$$

Since both this and the Hasimoto transformation are equivalent to the LIA, then (4.21) must have a solution which is equivalent to the Peregrine soliton, breathers and other solutions found under the Hasimoto map. The second term in Equation (4.20), αv_{ss}, is a diffusion term, which gives the disspation of the filament in the presence of the mutual friction parameter, $\alpha > 0$. The third term in (4.20), $-i\alpha U_3 v_s$, holds the influence of the normal fluid velocity, $|\mathbf{U}| = U_3$. This term may amplify the filament curvature, leading to local changes in the filament structure.

Since $0 \leq \alpha \leq 1$, a regular perturbation expansion may be attempted of the form

$$v(s,t) = v_0(s,t) + \alpha v_1(s,t) + O(\alpha^2). \tag{4.22}$$

Placing (4.22) into (4.20) yields

$$O(1): \quad \dot{v_0} = i\frac{\partial}{\partial s}\left\{\left(1-|v_0|^2\right)\frac{\partial}{\partial s}\left(\frac{v_0}{\sqrt{1-|v_0|^2}}\right)\right\}, \tag{4.23}$$

$$\begin{aligned} O(\alpha): \quad \dot{v_1} = i\frac{\partial}{\partial s}\Bigg\{ & \left(1-|v_0|^2\right)\frac{\partial}{\partial s}\left[\frac{v_1}{\sqrt{1-|v_0|^2}} - \frac{v_0(v_0^* v_1 + v_0 v_1^*)}{2(1-|v_0|^2)^{3/2}}\right] \\ & - (v_0^* v_1 + v_0 v_1^*)\frac{\partial}{\partial s}\left[\frac{v_0}{\sqrt{1-|v_0|^2}}\right]\Bigg\} + v_{0ss} - iU_3 v_{0s}. \end{aligned} \tag{4.24}$$

The $O(1)$ equation corresponds to a solution $v_0(s,t)$ for a classical vortex filament, while the $O(\alpha)$ equation represents the first-order correction.

While (4.24) is linear in v_1, it has complicated functional coefficients in terms of s and t, through the dependence on $v_0(s,t)$. As seen previously in Section 3.2 in Chapter 3, such equations can be very difficult to work with. Hence, an alternative approach must be sought out. Before doing this, the mathematical properties of the PDE (4.15) are studied, to get a better of understanding of the general behaviour of solutions.

4.4 Stability of Small Perturbations Along the Vortex Filaments

This section analyses the stability of small perturbations along line filaments under the PDE given in Equation (4.15). Since the models are complicated, some analytical results are provided prior to approximating a solution to Equation (4.20).

It is useful to consider small perturbations of the form

$$v(s,t) = \beta \mathrm{e}^{i(ks - c(t)) + r(t)}. \tag{4.25}$$

Then, neglecting $O(\beta^2)$ and higher order terms (assuming small amplitude

perturbations $|\beta| \ll 1$), Equation (4.15) gives

$$-i\dot{c}(t) + \dot{r}(t) = \left\{-(1-\alpha')k^2 - U_3\alpha' k\right\} i - \alpha(k^2 - U_3 k), \tag{4.26}$$

which implies, since $c(t)$ and $r(t)$ are real, that

$$c(t) = (1-\alpha')k^2 t + \alpha U_3 \alpha' k t, \tag{4.27}$$

$$r(t) = -\alpha k(k - U_3)t. \tag{4.28}$$

If $U_3 < k$, which means the normal fluid velocity is less than the wave number of the perturbation, then $r(t) < 0$ for $\alpha > 0, k > 0$ and the perturbations are stable. On the other hand, if $U_3 > k$, then the perturbations grow and the solution is unstable.

Therefore, in the small U_3 case, it is expected that solutions to the PDE will be stable, while for large U_3, they will be unstable [28, 29]. What this means is that, for small U_3, it is expected that there would be no drastic changes in the solutions between the quantum Hasimoto map and the PDE (4.15); hence, in this limit either model can be considered. On the other hand, when U_3 is large, the PDE in Equation (4.15) should be considered as the reliable model, since solutions to the quantum Hasimoto map are no longer representative. Another point to be noted is that α' does not qualitatively influence the structure of these perturbations, which adds further support to the assumption of neglecting α' and using Equation (4.20).

In summary, this simple stability analysis is an indication of when the influence of the normal fluid velocity can and cannot be neglected.

4.5 Influence of αv_{ss} term

In this section, the influence of the αv_{ss} term in Equation (4.20) is considered. It is worthwhile to consider a PDE given in conservation form as an initial value problem

$$\begin{aligned} &w_t = i\frac{\partial}{\partial s}\left(J[w]\right), \\ &w(s,0) = W(s), \quad s \in \mathbb{R}, \quad t > 0. \end{aligned} \tag{4.29}$$

Here J is a nonlinear differential operator in the spatial variable, s, with the property $(J[w])^* = J[w^*]$. It is useful to note that the complex conjugate w^* can be written as

$$w_t^* = -i\frac{\partial}{\partial s}\left(J[w^*]\right). \tag{4.30}$$

Multiplying Equation (4.29) by w^* and Equation (4.30) by w and then adding gives

$$w^* w_t + w w_t^* = i\left(w^*\frac{\partial}{\partial s}\left(J[w]\right) - w\frac{\partial}{\partial s}\left(J[w^*]\right)\right). \tag{4.31}$$

Yet, $w^* w_t + w w_t^* = \frac{\partial}{\partial t}(ww^*) = \frac{\partial}{\partial t}|w|^2$, so

$$\frac{\partial}{\partial t}|w|^2 = i\left(w^*\frac{\partial}{\partial s}\left(J[w]\right) - w\frac{\partial}{\partial s}\left(J[w^*]\right)\right). \tag{4.32}$$

The wave action or energy can be defined by

$$E(t) = \int_{-\infty}^{\infty} |w(s,t)|^2 ds. \tag{4.33}$$

Then, from Equation (4.32), assuming that $E(t)$ is sufficiently bounded, it can be found that

$$\begin{aligned}\frac{dE}{dt} &= \frac{\partial}{\partial t}\int_{-\infty}^{\infty} |w(s,t)|^2 ds \\ &= i\int_{-\infty}^{\infty}\left\{w^*\frac{\partial}{\partial s}\left(J[w]\right) - w\frac{\partial}{\partial s}\left(J[w^*]\right)\right\} ds \\ &= i\int_{-\infty}^{\infty}\left\{J[w^*]w_s - J[w]w_s^*\right\} ds,\end{aligned} \tag{4.34}$$

where the last line follows from an integration by parts and also from the assumption that $|w| \to 0$ as $|s| \to \infty$ and J is finite such that $|J[w]| < \infty$ as $|w| \to 0$, all sufficiently rapidly.

Equation (4.34) gives the change in the wave action over time or change in energy over time. Having dealt with the change in energy for the system (4.29), it is then worth considering a related system with a diffusion term added, that is

$$\begin{aligned}&\hat{w}_t = i\frac{\partial}{\partial s}\left(J[\hat{w}]\right) + \alpha\hat{w}_{ss}, \\ &\hat{w}(s,0) = W(s), \quad s \in \mathbb{R}, \quad t > 0.\end{aligned} \tag{4.35}$$

A remark to make is that the system (4.35) has the same initial condition as (4.29).

The analogous energy quantity can similarly be defined as

$$\hat{E}(t) = \int_{-\infty}^{\infty} |\hat{w}(s,t)|^2 ds. \tag{4.36}$$

Provided $\hat{E}(t)$ exists, and using the same technique as before,

$$\begin{aligned}\frac{d\hat{E}}{dt} &= \frac{\partial}{\partial t}\int_{-\infty}^{\infty} |\hat{w}(s,t)|^2 ds \\ &= i\int_{-\infty}^{\infty} \left\{J[\hat{w}^*]\hat{w}_s - J[\hat{w}]\hat{w}_s^*\right\} ds + \alpha \int_{-\infty}^{\infty} \left\{\hat{w}^*\hat{w}_{ss} + \hat{w}\hat{w}_{ss}^*\right\} ds.\end{aligned} \tag{4.37}$$

It can be noted that

$$\begin{aligned}&\int_{-\infty}^{\infty} \left\{\hat{w}^*\hat{w}_{ss} + \hat{w}\hat{w}_{ss}^*\right\} ds \\ &\quad = (w^*w_s + ww_s^*)|_{s=-\infty}^{s=+\infty} - \int_{-\infty}^{\infty} (w_s^*w_s + w_sw_s^*) ds \\ &\quad = 0 - 2\int_{-\infty}^{\infty} |w_s|^2 ds \\ &\quad = -2\int_{-\infty}^{\infty} |w_s|^2 ds.\end{aligned} \tag{4.38}$$

Therefore, this results in

$$\frac{d\hat{E}}{dt} = i\int_{-\infty}^{\infty} \left\{J[\hat{w}^*]\hat{w}_s - J[\hat{w}]\hat{w}_s^*\right\} ds - 2\alpha\int_{-\infty}^{\infty} |w_s|^2 ds. \tag{4.39}$$

Since both $w(s,0) = W(s)$ and $\hat{w}(s,0) = W(s)$, it can be concluded that $w(s,0) = \hat{w}(s,0)$. For small $t > 0$, it makes sense to then write

$$\frac{d\hat{E}}{dt} = \frac{dE}{dt} - 2\alpha\int_{-\infty}^{\infty} |w_s|^2 ds. \tag{4.40}$$

For all time t, $\int_{-\infty}^{\infty} |w_s|^2 ds \geq 0$, with equality to zero holding in the case of a constant solution in space. Then when $\alpha > 0$,

$$\frac{d\hat{E}}{dt} \leq \frac{dE}{dt}, \tag{4.41}$$

for small t. Hence, it has been shown that the inclusion of the term αw_{ss} in a general PDE of the form in Equation (4.35) results in faster initial (small time) decay of the energy or wave action of the solution.

For the PDE in Equation (4.20), it can be noted that

$$J[v] = \left(1 - |v|^2\right) \frac{\partial}{\partial s} \left(\frac{v}{\sqrt{1 - |v|^2}} \right) - \alpha U_3 v. \tag{4.42}$$

Therefore, the same analysis applies to the PDE (4.20) with initial condition $v(s, 0)$. Thus, this means that for the PDE (4.20), the αv_{ss} term results in more rapid dissipation of the energy of an initial state $v(s, 0)$. Therefore, for very small t, it is expected that there will be little change in the initial solution profile $v(s, 0)$; as t increases, more rapid dissipation will be observed. For the vortex filament, there will be more rapid dissipation of an initial disturbance or wave corresponding to $\alpha > 0$ rather than in the classical case when $\alpha = 0$.

This is consistent with what has been observed in the literature for Kelvin waves along quantum vortex filaments [28, 29]. For those cases, the dissipation manifests as a factor which scales as $\mathrm{e}^{-\alpha k^2 t} \sim \mathrm{e}^{-\alpha t}$, where k is the wave number ($k = O(1)$ in α). In other words, given a classical solution like $\psi_0(s, t)$, it is expected that the quantum solution will scale like $\psi(s, t) \sim \psi_0(s, t)\mathrm{e}^{-\alpha t}$ or also $v(s, t) \sim v_0(s, t)\mathrm{e}^{-\alpha t}$ (for $v(s, t)$ in the present model). This has the effect of smoothing the initial geometry over time, as the initial geometry for the classical case is given by $\psi_0(s, t)$ with the factor $\mathrm{e}^{-\alpha t}$ giving dissipation. A point worth making is that for warmer superfluid temperatures, α increases, resulting in faster dissipation. This makes sense, as the increase in temperature increases mutual friction, thus increasing the rate at which the quantum vortex filament dissipates.

4.6 Influence of $\alpha U_3 v_s$ term

Focus is then directed to the term $\alpha U_3 v_s$ in the PDE (4.20). Consideration of a scaling of the solution like $v(s, t) = V(s, t)\mathrm{e}^{i(ks - ct)}\mathrm{e}^{rt}$ ends up complicating the problem. Therefore, a multiplicative scaling does not seem useful. Similarly, an additive shift will not simplify the PDE. Clearly, this term must be dealt with differently.

It is necessary to seek out a transformation which does not modify the spatial structure in the nonlinear and the diffusion terms in the PDE (4.20). A wave-like

transformation can be considered such as

$$v(s,t) = V(s - ct, t). \tag{4.43}$$

This is motivated by the fact that the normal fluid velocity may shift or push the structure of the vortex filament in some way.

Denoting $\xi = s - ct$ gives $v(s,t) = V(\xi, t)$ and

$$\dot{v} = V_t - cV_\xi, \quad v_s = V_\xi, \quad v_{ss} = V_{\xi\xi}. \tag{4.44}$$

Substituting these into the PDE (4.20) leads to

$$V_t - cV_\xi = i\frac{\partial}{\partial \xi}\left\{\left(1 - |V|^2\right)\frac{\partial}{\partial \xi}\left(\frac{V}{\sqrt{1-|V|^2}}\right)\right\} + \alpha V_{\xi\xi} - i\alpha U_3 V_\xi. \tag{4.45}$$

Picking $c = i\alpha U_3$ gives

$$V_t = i\frac{\partial}{\partial \xi}\left\{\left(1 - |V|^2\right)\frac{\partial}{\partial \xi}\left(\frac{V}{\sqrt{1-|V|^2}}\right)\right\} + \alpha V_{\xi\xi}. \tag{4.46}$$

It can be seen that Equation (4.46) and Equation (4.20) are exactly the same by regarding ξ as a spatial variable and if $U_3 = 0$. Therefore, if $v(s,t) = \hat{v}(s,t)$ is a particular solution to (4.20) when $U_3 = 0$, then $V(\xi,t) = \hat{v}(\xi,t) = \hat{v}(s - i\alpha U_3 t, t)$ is a solution to (4.46). In other words, having a solution $\hat{v}(s,t)$ to (4.20) when $U_3 = 0$, enables a solution $v(s,t)$ to (4.20) when $U_3 \neq 0$ to be obtained by taking the function $v(s,t) = \hat{v}(s - i\alpha U_3 t, t)$. This is a rather elegant and remarkably simple way to account for the normal fluid velocity U_3. Therefore, with the transformation $v(s,t) = V(s - i\alpha U_3 t, t)$, only the PDE (4.46) needs to be solved.

4.7 Approximating Quantum Vortex Filament Dynamics from Classical LIA Solutions

The influence of both the terms αv_{ss} and $-i\alpha U_3 v_s$ on the solutions to the PDE (4.20) are now known. Indeed, from the discussion of the term $-i\alpha U_3 v_s$, it is now known that a solution $v(s,t) = V(\xi,t)$ should be considered, where $\xi = s - i\alpha U_3 t$ and $V(\xi,t)$ is a solution of Equation (4.46). Yet, (4.46) is of the form (4.35) and from the

discussion of the term αv_{ss}, it is now known that a solution of (4.46) should scale like $V(\xi,t) = \tilde{V}(\xi,t)\mathrm{e}^{-\alpha t}$, where $\tilde{V}(\xi,t)$ satisfies

$$\tilde{V}_t = i\frac{\partial}{\partial\xi}\left\{\left(1-|\tilde{V}|^2\right)\frac{\partial}{\partial\xi}\left(\frac{\tilde{V}}{\sqrt{1-|\tilde{V}|^2}}\right)\right\}, \tag{4.47}$$

which is just the classical LIA in the framework of Equation (4.15). Therefore, if $\tilde{V}(\xi,t)$ is any classical LIA solution, then

$$v(s,t) = \tilde{V}(s - i\alpha U_3 t, t)\mathrm{e}^{-\alpha t}, \tag{4.48}$$

is a solution (up to scaling and higher order terms in α) of the quantum model (4.20). As such, the solution (4.48) will adequately approximate the qualitative features of a solution to (4.20) and hence of a solution to (4.15).

For any such classical solution $\tilde{V}(\xi,t)$, the quantum vortex filament dynamics can therefore be approximated from the tangent vector in $((y,z,x)$ coordinates) as

$$\mathbf{t}(s,t) \approx \begin{bmatrix} \frac{1}{2}\left\{\tilde{V}(s-i\alpha U_3 t,t) + \tilde{V}^*(s-i\alpha U_3 t,t)\right\}\mathrm{e}^{-\alpha t} \\ \frac{1}{2i}\left\{\tilde{V}(s-i\alpha U_3 t,t) - \tilde{V}^*(s-i\alpha U_3 t,t)\right\}\mathrm{e}^{-\alpha t} \\ \sqrt{1-|\tilde{V}(s-i\alpha U_3 t,t)|^2\mathrm{e}^{-2\alpha t}} \end{bmatrix}. \tag{4.49}$$

By then integrating in s, the vortex filament curve in $\mathbb{R}^3$ can be recovered which gives the Cartesian coordinates (x,y,z) for the vortex filament curve as

$$\mathbf{r}(s,t) \approx \begin{bmatrix} \int_0^s \sqrt{1-|\tilde{V}(\sigma-i\alpha U_3 t,t)|^2\mathrm{e}^{-2\alpha t}}\,d\sigma \\ \frac{1}{2}\mathrm{e}^{-\alpha t}\int_0^s \left\{\tilde{V}(\sigma-i\alpha U_3 t,t) + \tilde{V}^*(\sigma-i\alpha U_3 t,t)\right\}d\sigma \\ \frac{1}{2i}\mathrm{e}^{-\alpha t}\int_0^s \left\{\tilde{V}(\sigma-i\alpha U_3 t,t) - \tilde{V}^*(\sigma-i\alpha U_3 t,t)\right\}d\sigma \end{bmatrix}. \tag{4.50}$$

4.8 Quantum Curvature and Torsion

Given a solution $v(s,t)$ to Equation (4.15), differentiation of Equation (4.2) gives

$$\mathbf{t}_s = \left(\frac{v_s + v_s^*}{2}, \frac{v_s - v_s^*}{2i}, \frac{\partial}{\partial s}\left(\sqrt{1-|v^2|}\right)\right). \tag{4.51}$$

The curvature $\kappa(s,t)$ is then given by

$$\begin{aligned}\kappa(s,t) &= |\mathbf{t}_s| \\ &= \sqrt{\left(\frac{v_s + v_s^*}{2}\right)^2 + \left(\frac{v_s - v_s^*}{2i}\right)^2 + \left(\frac{\partial}{\partial s}\left(\sqrt{1-|v^2|}\right)\right)^2} \\ &= \sqrt{v_s v_s^* + \left(\frac{\partial}{\partial s}\left(\sqrt{1-|v^2|}\right)\right)^2} \\ &= \sqrt{|v_s|^2 + \left(\frac{\partial}{\partial s}\left(\sqrt{1-|v^2|}\right)\right)^2}. \end{aligned} \tag{4.52}$$

Now, for $v(s,t)$ a solution of PDE (4.20), it has been shown that $v(s,t) \approx V(s - i\alpha U_3 t, t)\mathrm{e}^{-\alpha t}$, where V corresponds to a classical LIA solution. Then,

$$\begin{aligned}\kappa(s,t) &\approx \mathrm{e}^{-\alpha t}\sqrt{|V|^2 + \left(\frac{\partial}{\partial \xi}\left(\sqrt{1-|V^2|}\right)\right)^2} \\ &= \mathrm{e}^{-\alpha t}|\psi_0(s - i\alpha U_3 t, t)| \\ &= \mathrm{e}^{-\alpha t}\kappa_0(s,t). \end{aligned} \tag{4.53}$$

A similar result implies $\tau(s,t) \approx \tau_0(s,t)$.

Here ψ_0 is the $O(1)$ term in the quantum Hasimoto transformation; it is a solution for a classical vortex filament. This means that ψ_0 is a solution of the cubic NLS equation. κ_0 and τ_0 denote the calculated curvature and torsion corresponding to $\psi(s - i\alpha U_3 t, t)$ and both are real-valued quantities.

Therefore, once a solution to the classical LIA is known, Equation (4.48) can be used to approximate a solution to the quantum LIA for any small $\alpha \ll 1$ and $U_3 \in \mathbb{R}$, including $U_3 = 0$. Thus, this model holds solutions of the Chapter 3 model as special cases. In what follows, solutions are demonstrated for the Peregrine soliton and Akhmediev breather along vortex filaments with quantum effects using Equation (4.48).

4.9 Peregrine Soliton on a Quantum Vortex Filament

To obtain the quantum solution $\psi(s,t)$ for a Peregrine soliton along a vortex filament, the classical solution is denoted as $\psi_0(s,t)$ where

$$\psi_0(s,t) = \sqrt{2|\omega|}\Big(1 - \frac{4(1+2|\omega|it)}{1+4[2|\omega|s^2+\omega^2t^2]}\Big)\mathrm{e}^{-i\omega t}, \tag{4.54}$$

is a solution to the cubic NLS equation. Then, $\psi(s,t)$ for a Peregrine soliton on a quantum vortex filament which agrees with the classical Peregrine soliton at $t=0$, must be given by

$$\begin{aligned}\psi(s,t) &= \kappa(s,t)\mathrm{e}^{i\int_0^s \tau(\hat{s},t)d\hat{s}} \\ &= \sqrt{2|\omega|}\Big(1 - \frac{4(1+2|\omega|it)}{1+4[2|\omega|(s-i\alpha U_3 t)^2+\omega^2t^2]}\Big)\mathrm{e}^{-i\omega t}\mathrm{e}^{-\alpha t} \\ &= \sqrt{2|\omega|}\Big(1 - \frac{4(1+2|\omega|it)}{1+4\left[\{2|\omega|s^2-2|\omega|\alpha^2U_3^2t^2+\omega^2t^2\}\right]-4|\omega|\alpha U_3 t\, i}\Big)\mathrm{e}^{-i\omega t}\mathrm{e}^{-\alpha t}.\end{aligned} \tag{4.55}$$

By splitting Equation (4.55) to rewrite it in terms of its real and imaginary components as $\psi(s,t) = R(s,t) + iI(s,t)$ as done for the classical case in Section 2.5 in Chapter 2, both $\kappa(s,t)$ and $\tau(s,t)$ can be determined similarly using Equations (2.60) and (2.61).

Calculating $R(s,t)$ and $I(s,t)$ and using Equations (2.60) and (2.61), solutions for the curvature, $\kappa(s,t)$, and torsion, $\tau(s,t)$, of a quantum Peregrine soliton take the form

$$\begin{aligned}\kappa(s,t) = \sqrt{2}\Bigg\{\Big\{\omega\mathrm{e}^{-2\alpha t}\Big[&-8\omega\Big(2s^2\left(4t^2\omega\left(2\alpha^2U_3^2-\omega\right)+3\right) \\ &+t^2\omega\left(2t^2\left(2\alpha^2U_3^2+\omega\right)^2+5\right) \\ &-6\alpha^2t^2U_3^2+32\alpha st^2U_3\omega+8s^4\omega\Big)-9\Big]\Big\} \\ &\Big/\Big\{-16s^2\omega\left(4t^2\omega\left(\omega-2\alpha^2U_3^2\right)+1\right) \\ &+\left(4t^2\omega\left(2\alpha^2U_3^2+\omega\right)+1\right)^2+64s^4\omega^2\Big\}\Bigg\},\end{aligned} \tag{4.56}$$

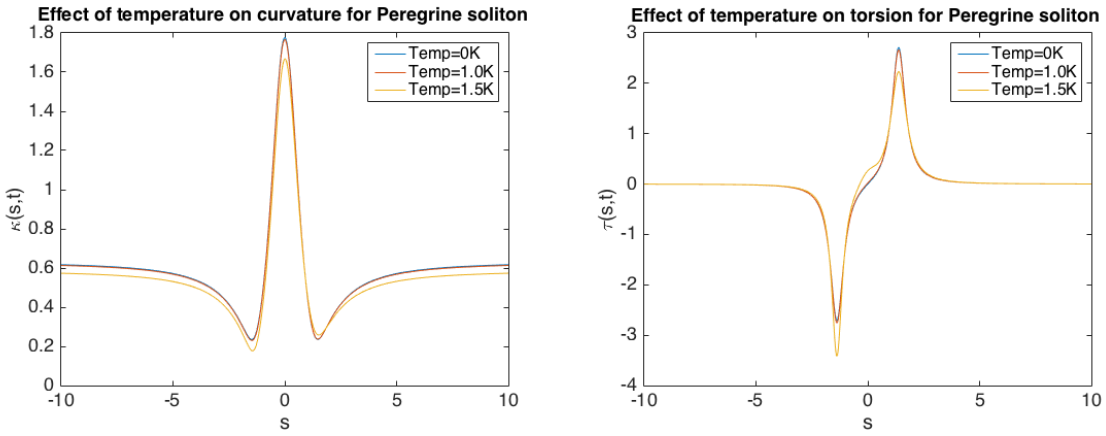

(a) (b)

Figure 4.1: (a): Effect of temperature on curvature for quantum Peregrine soliton; (b): Effect of temperature on torsion for quantum Peregrine soliton (temperatures corresponding to $\alpha = 0$ for 0K, $\alpha = 0.006$ for 1K and $\alpha = 0.073$ for 1.5K with $\omega = -0.2, t = 1, U_3 = 1$).

and

$$\begin{aligned}\tau(s,t) = \Bigg\{ & 64t\omega\Big[64\alpha^5 t^4 U_3^5\omega^2 - 384\alpha^4 s t^4 U_3^4\omega^3 - 16\alpha^3 t^2 U_3^3\omega\left(8s^2\omega + 4t^2\omega^2 + 1\right) \\ & - 32\alpha^2 s t^2 U_3^2\omega^2\left(8s^2\omega + 4t^2\omega^2 + 1\right) \\ & - \alpha U_3\left(192s^4\omega^2 + 16s^2\left(4t^2\omega^3 + \omega\right) + 3\left(4t^2\omega^2 + 1\right)^2\right) \\ & + 2s\omega\left(-8s^2\omega + 4t^2\omega^2 + 1\right)^2\Big]\Bigg\} \\ & \Big/\Big[-16s^2\omega\left(4t^2\omega\left(\omega - 2\alpha^2 U_3^2\right) + 1\right) + \left(4t^2\omega\left(2\alpha^2 U_3^2 + \omega\right) + 1\right)^2 + 64s^4\omega^2\Big] \\ & \times\Big[8\omega\Big(2s^2\left(4t^2\omega\left(2\alpha^2 U_3^2 - \omega\right) + 3\right) + t^2\omega\left(2t^2\left(2\alpha^2 U_3^2 + \omega\right)^2 + 5\right) \\ & - 6\alpha^2 t^2 U_3^2 + 32\alpha s t^2 U_3\omega + 8s^4\omega\Big) + 9\Big]. \end{aligned} \tag{4.57}$$

Figures 4.1(a) and 4.1(b) highlight the variation of both curvature and torsion with temperature for the quantum Peregrine soliton and it can be observed that as expected, for higher values of temperature governed by the parameter α, there is faster dissipation of both the curvature and torsion values by the factor $\mathrm{e}^{-\alpha t}$, leading to a drop in the values. This is reasonable, since an increase in temperature causes higher mutual friction, thereby increasing the dissipation rate for quantum filaments.

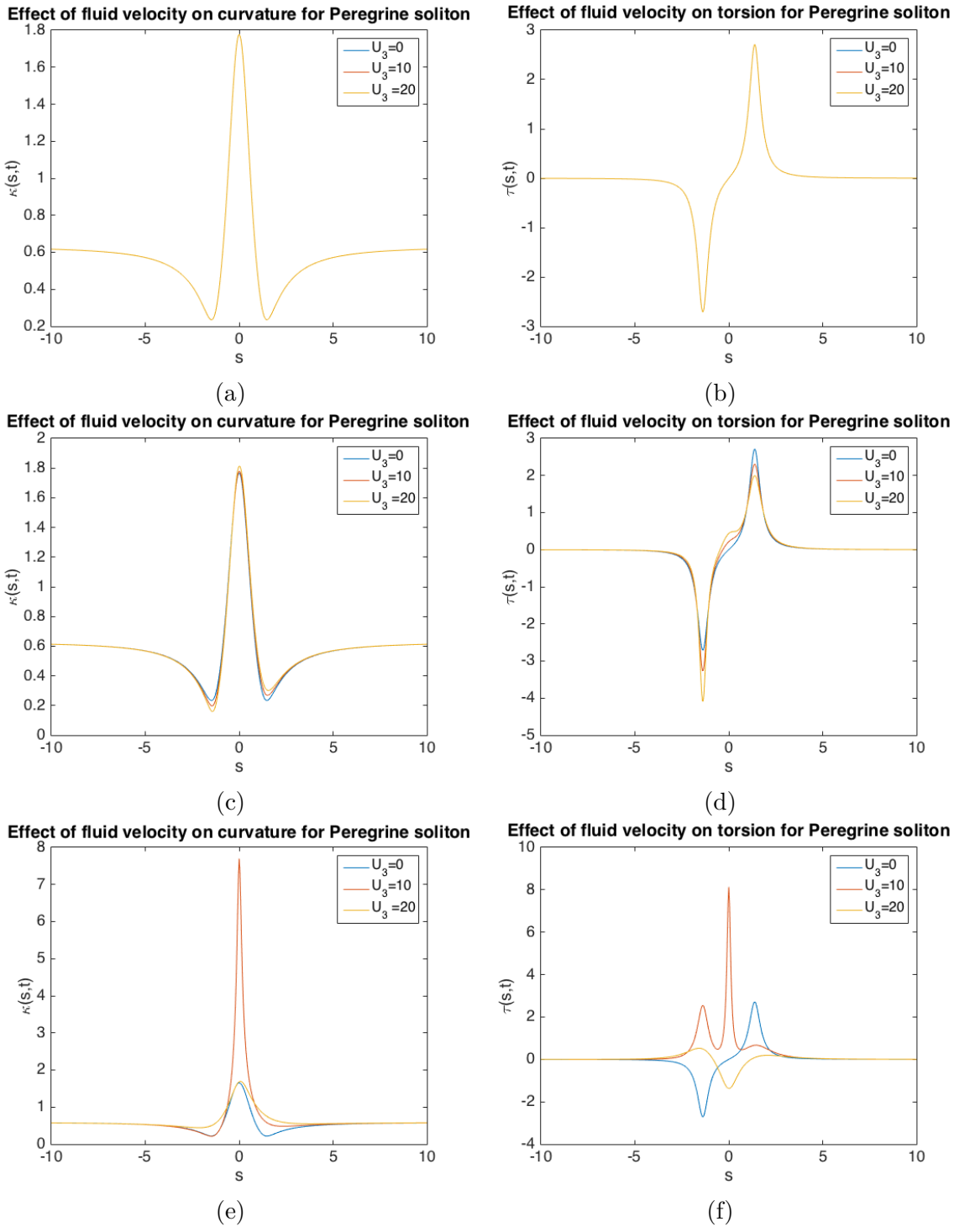

Figure 4.2: Effect of normal fluid velocity on curvature and torsion respectively for quantum Peregrine soliton at temperatures of (a), (b): 0K; (c), (d): 1.0K; (e), (f): 1.5K ($\omega = -0.2, t = 1$).

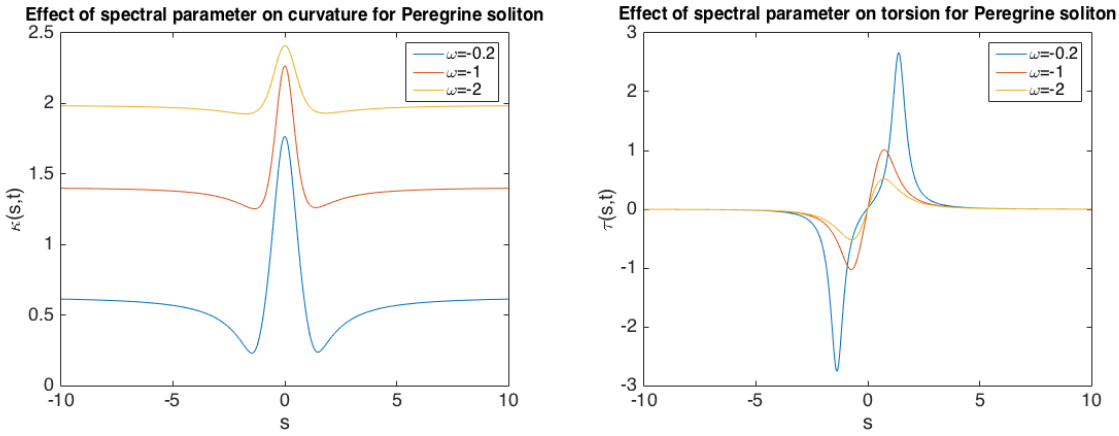

(a) (b)

Figure 4.3: (a): Effect of spectral parameter on curvature for quantum Peregrine soliton; (b): Effect of spectral parameter on torsion for quantum Peregrine soliton ($\alpha = 0.006, t = 1, U_3 = 1$).

Figure 4.2 depicts the effect of normal fluid velocity U_3 on both curvature and torsion for specific values of temperatures: 0K in Figures 4.2(a) and 4.2(b), 1.0K in Figures 4.2(c) and 4.2(d) and 1.5K in Figures 4.2(e) and 4.2(f). It can be observed that at 0K corresponding to the classical case, the plots for different U_3 are all perfectly superimposed on each other, which is indicative of the stability of the solutions in the classical regime with U_3 having no effect on the shape of the curves. However, in the quantum regime, the solutions are indeed influenced by the normal fluid velocity and are seen to be amplified for $U_3 = 10$, until they subsequently subside back to the classical plot for $U_3 = 0$.

Figures 4.3(a) and 4.3(b) highlight the effect of the spectral parameter ω on both curvature and torsion for the quantum Peregrine soliton. It is evident that ω influences the shape/amplitude of the wave, with higher values of $|\omega|$ leading to upward shifts in the curves for both curvature and torsion.

Thus, it can be deduced that the temperature parameter α influences the dissipation rate of the solutions and corresponds to the second term, αv_{ss}, in the PDE (4.20) in Section 4.3, while the normal fluid velocity U_3 tends to affect the stability of the solutions causing local changes in the filament structure and is governed by the third term, $-i\alpha U_3 v_s$, in (4.20). Finally, the spectral parameter ω leads to changes in the shape and amplitude of the curves.

The beauty of the methodology of the $\mathbf{U} \neq \mathbf{0}$ map adopted in Chapter 4 is that

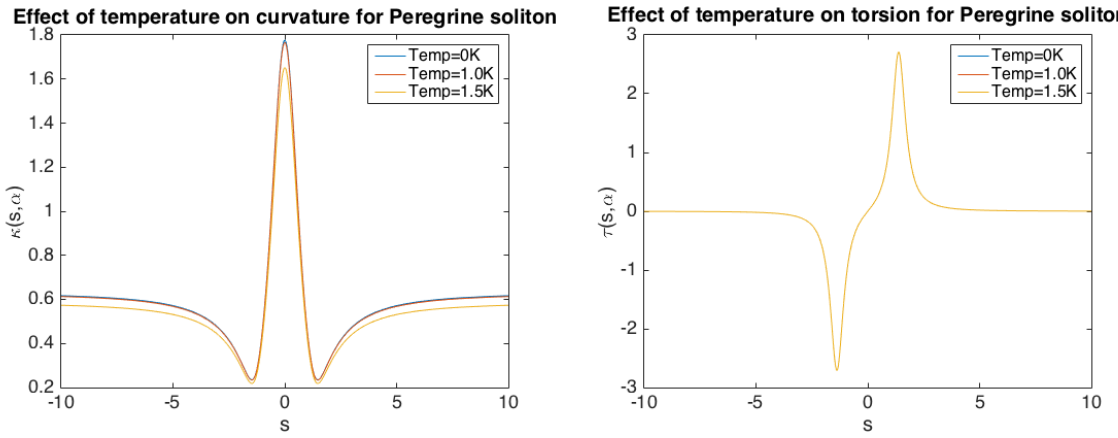

(a) (b)

Figure 4.4: (a), (b): Effect of temperature on curvature and torsion for quantum Peregrine soliton when $U_3 = 0$ (temperatures corresponding to $\alpha = 0$ for 0K, $\alpha = 0.006$ for 1K and $\alpha = 0.073$ for 1.5K with $\omega = -0.2, t = 1$).

it enables the solutions for $U_3 = 0$ for $\alpha > 0$ to be recovered, which could not be obtained using the quantum Hasimoto map formulation in Chapter 3. This is shown in Figures 4.4(a) and 4.4(b), which show the effect of the temperature parameter α on curvature and torsion when $U_3 = 0$. In the absence of normal fluid velocity effects, the quantum model is seen to show only slight deviations in the curvature plots, while the torsion remains unchanged.

4.10 Akhmediev Breather on a Quantum Vortex Filament

To obtain the quantum solution $\psi(s,t)$ for a spatially-periodic Akhmediev breather on a vortex filament, the classical solution is denoted as $\psi_0(s,t)$ where

$$\psi_0(s,t) = \bar{\kappa_0} \mathrm{e}^{i\left(\frac{\bar{\kappa_0}^2 t}{2} + \bar{\tau_0} s + \left(\bar{\kappa_0}^2 - \bar{\tau_0}^2\right) t\right)} \frac{\cosh(\Omega \bar{\kappa_0}^2 t/4 - 2i\phi) - \cos(\phi)\cos(k\bar{\kappa_0} s/2 - k\bar{\tau_0}\bar{\kappa_0} t)}{\cosh(\Omega \bar{\kappa_0}^2 t/4) - \cos(\phi)\cos(k\bar{\kappa_0} s/2 - k\bar{\tau_0}\bar{\kappa_0} t)}, \tag{4.58}$$

where, $k = 2\sin(\phi)$ and $\Omega = 2\sin(2\phi)$. Then, $\psi(s,t)$ for an Akhmediev breather on a quantum vortex filament which agrees with the classical Akhmediev breather at

$t = 0$, must be given by

$$\begin{aligned}\psi(s,t) &= \kappa(s,t)\mathrm{e}^{i\int_0^s \tau(\hat{s},t)d\hat{s}} \\ &= \bar{\kappa_0}e^{it\left(\bar{\kappa_0}^2-\bar{\tau_0}^2\right)+\frac{1}{2}i\bar{\kappa_0}^2t+i\bar{\tau_0}(s-i\alpha U_3 t)-\alpha t} \\ &\quad\times\Bigg(-\cos(\phi)\cos(\bar{\kappa_0}(s-i\alpha U_3 t)\sin(\phi)-2\bar{\kappa_0}\bar{\tau_0}t\sin(\phi)) \\ &\quad+\cos\left(2\phi+\frac{1}{2}i\bar{\kappa_0}^2t\sin(2\phi)\right)\Bigg)\Bigg/\Bigg(\cosh\left(\frac{1}{2}\bar{\kappa_0}^2t\sin(2\phi)\right) \\ &\quad-\cos(\phi)\cos(\bar{\kappa_0}(s-i\alpha U_3 t)\sin(\phi)-2\bar{\kappa_0}\bar{\tau_0}t\sin(\phi))\Bigg). \end{aligned} \tag{4.59}$$

By splitting Equation (4.59) to rewrite it in terms of its real and imaginary components as $\psi(s,t) = R(s,t) + iI(s,t)$ as done for the classical case in Section 2.5 in Chapter 2, both $\kappa(s,t)$ and $\tau(s,t)$ can be determined similarly using using Equations (2.60) and (2.61).

Calculating $R(s,t)$ and $I(s,t)$ and using Equations (2.60) and (2.61), solutions for the curvature, $\kappa(s,t)$, and torsion, $\tau(s,t)$, of a quantum Peregrine soliton take the form

$$\kappa(s,t) = \bar{\kappa_0}\mathrm{e}^{-\alpha t(1-U_3)}\sqrt{R_1^2+R_2^2}, \tag{4.60}$$

and

$$\tau(s,t) = \frac{\left(R_1\cos\theta + R_2\sin\theta\right)J_1 - \left(R_1\sin\theta - R_2\cos\theta\right)J_2}{R_1^2+R_2^2}, \tag{4.61}$$

where $J_1(s,t)$, $J_2(s,t)$, $R_1(s,t)$, $R_2(s,t)$ and $\theta(s,t)$ are all real functions given by

$$J_1(s,t) = R_1\bar{\tau_0}\cos\theta + \sin\theta\frac{dR_1}{ds} - \cos\theta\frac{dR_2}{ds} + R_2\bar{\tau_0}\sin\theta, \tag{4.62}$$

$$J_2(s,t) = -R_1\bar{\tau_0}\sin\theta + \cos\theta\frac{dR_1}{ds} + \sin\theta\frac{dR_2}{ds} + R_2\bar{\tau_0}\cos\theta, \tag{4.63}$$

$$\begin{aligned}R_1(s,t) &= \Big(\left(\cosh d - \cos\phi\cos f\cosh g\right)^2 + \cos^2\phi\sin^2 f\sinh^2 g \\ &\quad-\sin(2\phi)\sinh d\cos\phi\sin f\sinh g\Big) \\ &\quad\Big/\Big(\left(\cosh d - \cos\phi\cos f\cosh g\right)^2 + \cos^2\phi\sin^2 f\sinh^2 g\Big), \end{aligned} \tag{4.64}$$

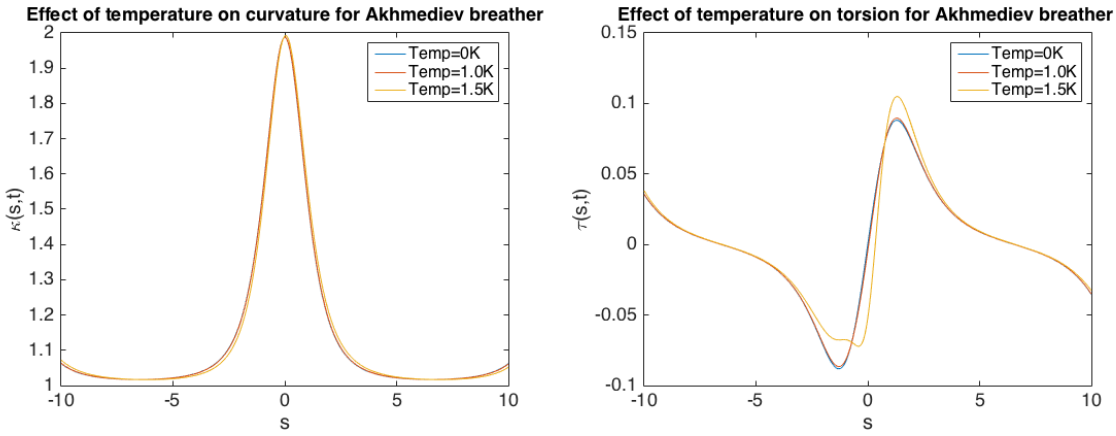

(a) (b)

Figure 4.5: (a): Effect of temperature on curvature for quantum Akhmediev breather; (b): Effect of temperature on torsion for quantum Akhmediev breather (temperatures corresponding to $\alpha = 0$ for 0K, $\alpha = 0.006$ for 1K and $\alpha = 0.073$ for 1.5K with $\bar{\kappa_0} = 1, \bar{\tau_0} = 0, \phi = 0.5, t = 1, U_3 = 1$).

$$R_2(s,t) = \frac{(\cosh d - \cos\phi \cos f \cosh g)\sin(2\phi)\sinh d}{(\cosh d - \cos\phi\cos f\cosh g)^2 + \cos^2\phi \sin^2 f \sinh^2 g}, \tag{4.65}$$

$$\theta(s,t) = t\left(\bar{\kappa_0}^2 - \bar{\tau_0}^2\right) + \frac{1}{2}\bar{\kappa_0}^2 t + \bar{\tau_0} s, \tag{4.66}$$

with $d = \frac{1}{2}\bar{\kappa_0}^2 t \sin 2\phi$, $f = 2\bar{\kappa_0}\bar{\tau_0} t \sin\phi - \bar{\kappa_0} s \sin\phi$, and $g = \alpha t U_3 \sin\phi$.

Figures 4.5(a) and 4.5(b) highlight the variation of both curvature and torsion with temperature for the quantum Akhmediev breather. It can be observed that for higher values of α, the curvature plot for the Akhmediev breather, unlike that of the Peregrine soliton, does not show any significant variation with temperature, with the curves perfectly superimposed on each other. The torsion plot on the other hand shows greater fluctuation at higher temperatures, as evident from the curve at 1.5K.

Figure 4.6 depicts the effect of normal fluid velocity U_3 on both curvature and torsion for specific values of temperatures: 0K in Figures 4.6(a) and 4.6(b), 1.0K in Figures 4.6(c) and 4.6(d) and 1.5K in Figures 4.6(e) and 4.6(f). It can be observed that at 0K corresponding to the classical case, the plots for different U_3 are all perfectly superimposed on each other, which is indicative of the stability of the solutions in the classical regime with U_3 having no effect on the shape of the curves. However, in the quantum regime, the solutions are indeed influenced by the normal fluid velocity and are seen to be gradually amplified reaching a peak amplitude for $U_3 = 20$ at 1.5K.

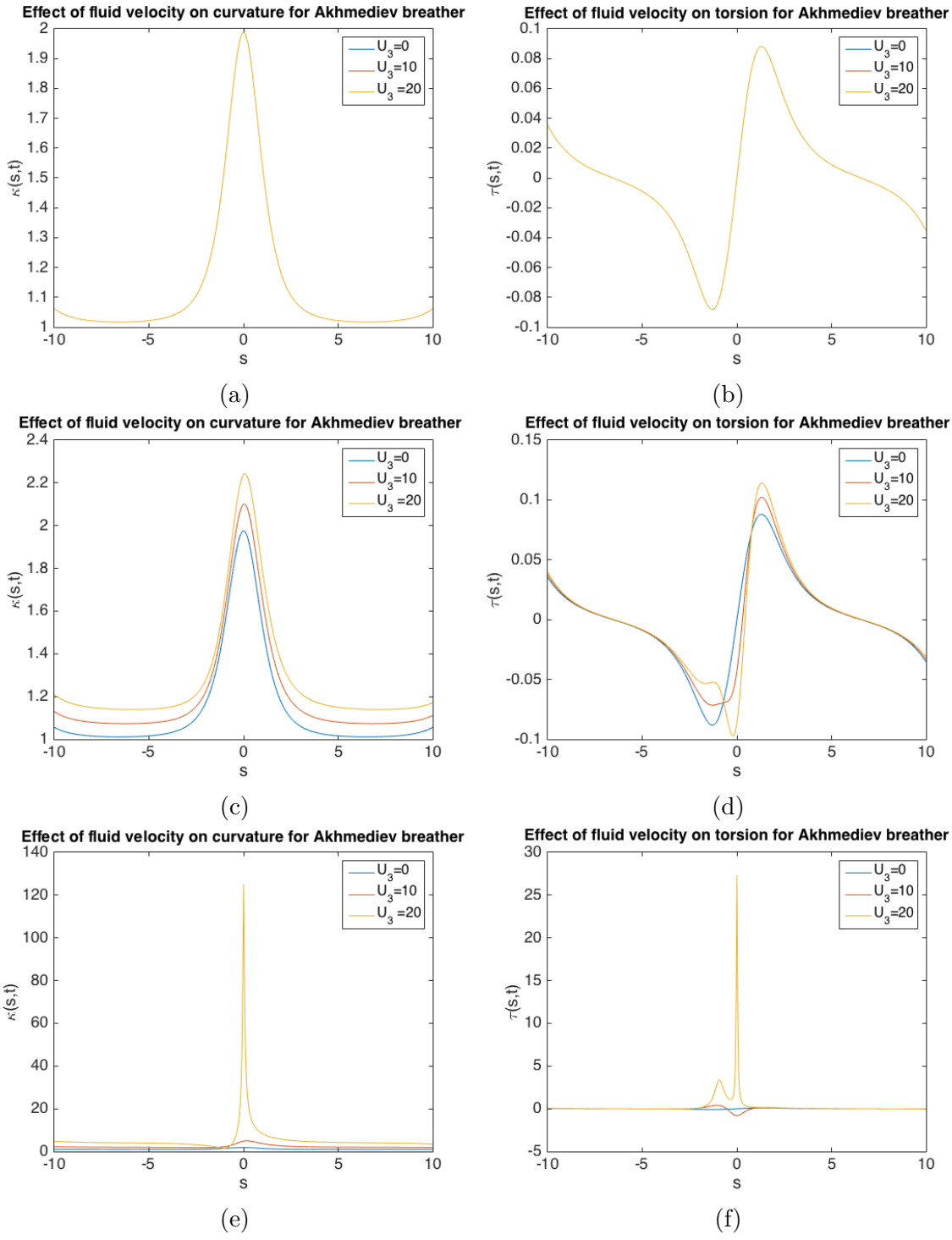

Figure 4.6: Effect of normal fluid velocity on curvature and torsion respectively for quantum Akhmediev breather at temperatures of (a), (b): 0K; (c), (d): 1.0K; (e), (f): 1.5K ($\bar{\kappa_0} = 1, \bar{\tau_0} = 0, \phi = 0.5, t = 1$).

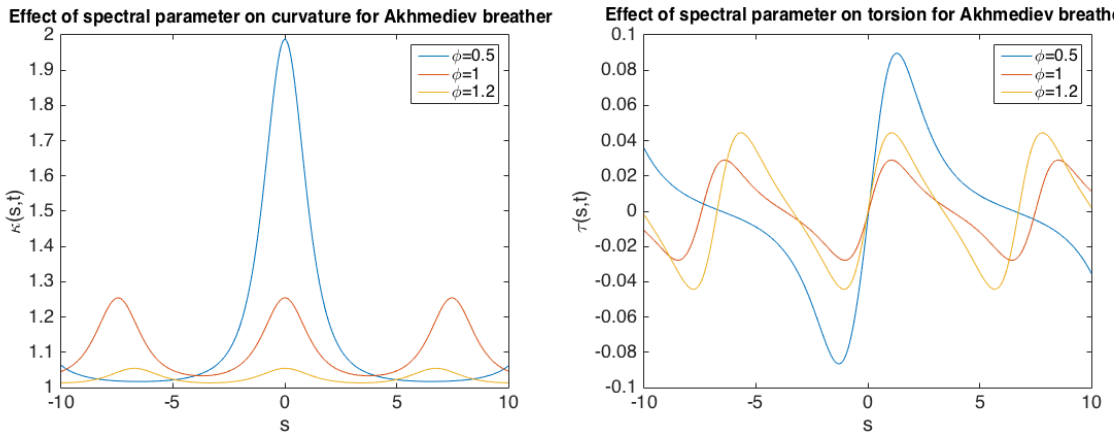

(a) (b)

Figure 4.7: (a): Effect of spectral parameter on curvature for quantum Akhmediev breather; (b): Effect of spectral parameter on torsion for quantum Akhmediev breather ($\bar{\kappa_0} = 1, \bar{\tau_0} = 0, \alpha = 0.006, t = 1, U_3 = 1$).

Figures 4.7(a) and 4.7(b) highlight the effect of the spectral parameter ϕ on both curvature and torsion for the quantum Akhmediev breather. It is evident that ϕ influences the shape/amplitude of the wave, with the curvature plots subsiding for higher values of ϕ, while the torsion plot reaches a minimum amplitude for $\phi = 1$.

Thus, it can be deduced that unlike the Peregrine soliton, the mutual friction parameter α does not influence the dissipation rate of the solutions significantly, though the normal fluid velocity U_3 does still tend to affect the stability of the solutions causing local changes in the filament structure. Finally, the spectral parameter ϕ does indeed lead to prominent changes in the shape and amplitude of the curves.

As mentioned earlier in Section 4.9, the beauty of the methodology of the $\mathbf{U} \neq \mathbf{0}$ map adopted in Chapter 4 is that it enables the solutions for $U_3 = 0$ for $\alpha > 0$ to be recovered, which could not be obtained using the quantum Hasimoto map formulation in Chapter 3. This is shown in Figures 4.8(a) and 4.8(b) for the Akhmediev breather, which show the effect of the temperature parameter α on curvature and torsion when $U_3 = 0$. In the absence of normal fluid velocity effects, the quantum model is seen to show greater deviations in the curvature plots with temperature than when $U_3 \neq 0$, while the torsion remains unchanged.

As discussed in Section 2.4, the curvature and torsion results discussed here could be taken and used to plot the vortex filament in Cartesian coordinates. However, the

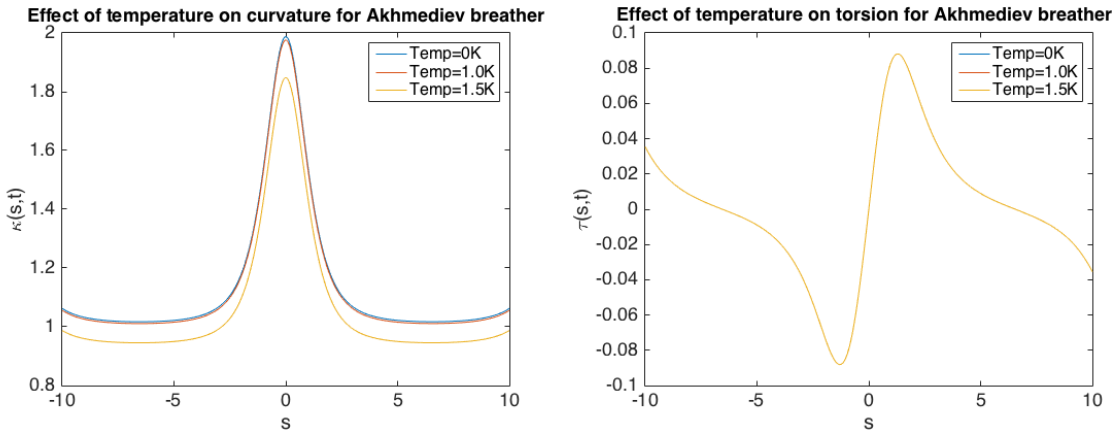

(a) (b)

Figure 4.8: (a), (b): Effect of temperature on curvature and torsion for quantum Akhmediev breather when $U_3 = 0$ (temperatures corresponding to $\alpha = 0$ for 0K, $\alpha = 0.006$ for 1K and $\alpha = 0.073$ for 1.5K with $\bar{\kappa_0} = 1, \bar{\tau_0} = 0, \phi = 0.5, t = 1$).

curvature and torsion hold the salient geometric features of the solutions (the reader is directed to Section 2.4 and also Appendix A); hence it is sufficient to primarily study both quantities. Section 2.4 can then be used to recover the vortex filament curves from the curvature and torsion solutions given here.

Chapter 5

Discussion and Physical Relevance

The primary objective of this dissertation was to study the motion of a single vortex filament within a classical/quantum fluid through a mapping of its three-dimensional position vector to a scalar curvature-torsion domain to unravel its dynamical characteristics. The principal model adopted for this purpose was the LIA formulation, which serves as a local approximation to the more generalised non-local Biot-Savart equation. The reason for selecting this model, besides its simplification of an extremely complicated non-local problem, lies in its ability to enable a qualitative comparison of quantum and classical fluid LIA solutions [2]. The mathematical analysis presented in Chapters 2 through 4 was applied to two specific types of nonlinear wave solutions: the Peregrine soliton and the Akhmediev breather.

The behaviour of a vortex filament in a classical fluid such as water comprised the bulk of Chapter 2. Solutions were obtained via a Hasimoto mapping of the classical form of the LIA to a cubic NLS equation [1]. The spatially-symmetric curvature plots obtained demonstrated good agreement with those present in literature sources, namely [5] for the Peregrine soliton and [26] for the Akhmediev breather. In both cases, the peak amplitude was achieved at the origin $s = 0$, with the curves decaying to constant values as $s \to \infty$. On the other hand, the rotationally-symmetric torsion plots were characterised by two spikes on either side of the origin. The transient nature of rogue wave behaviour that was expected was aptly depicted by the classical case, with the decay of solutions as $t \to \infty$.

The model was then generalised further in Chapter 3 to account for the effect of mutual friction that a quantised vortex at finite temperatures is subjected to in the presence of a superfluid such as He II. This was done through the introduction of a

temperature-dependent parameter α to yield a simplified version of the quantum LIA obtained by Schwarz [10] that mapped to a complex GLE equation with an extra dissipation term. The underlying assumption of the quantum Hasimoto formulation [2] employed, involved neglecting the effect of normal fluid velocity on the vortex filament by setting $\mathbf{U} = \mathbf{0}$. This model prescribed a regular perturbation expansion in $\psi(s,t)$ with an additional first-order correction up to $O(\alpha)$ to the already determined classical solution. However, it turned out to be rather difficult to obtain solutions for the Peregrine soliton and Akhemediev breather with this model, due to the singularity of the variable coefficients in the equations to be solved.

This motivated the need to formulate an alternative mapping model that would be independent of the quantum Hasimoto transformation to yield the required quantum solutions and this formed the core of Chapter 4. The complete generalised form of Schwarz's quantum LIA [10] that accounted for normal fluid velocity $\mathbf{U} \neq \mathbf{0}$ was used to map a newly defined complex function $v(s,t)$ to an entirely distinct PDE. It was found that this method was successful in providing quantum solutions that agreed well with the expected effects of temperature, normal fluid velocity and spectral parameter on rogue wave behaviour. It was observed that the the temperature parameter α led to dissipation of the solutions in a manner proportional to $\mathrm{e}^{-\alpha t}$ in the quantum regime when $\alpha > 0$, while also confirming the hypothesis of zero dissipation in the classical regime when $\alpha = 0$. The fluid velocity U_3 influenced the stability of solutions in the quantum domain, with an increase in instability for larger values of U_3. Finally, the spectral parameters ω and ϕ for the Peregrine soliton and Akhmediev breathers, respectively, were found to affect the shape/amplitude of the curves, consistent with plots obtained in [5]. The ingenuity of this model was such that it provided a successful way of easily recovering the solutions for the special $\mathbf{U} = \mathbf{0}$ case from Chapter 3.

Finally, it is worth pointing out that the utility of the LIA solutions obtained is not simply restricted to a theoretical framework, but can also aid with experimental work to demonstrate the existence of rogue waves as done in [30]. For example, limiting the temperature domain for a vortex filament to 2K would be useful to completely analyse the behaviour of a vortex filament in a quantum fluid such as He II, since He II possesses superfluid properties only within $0K < T < 2K$. Thus, experimentalists can design experiments to ascertain the influence of physical variables such as temperature and normal fluid velocity on rogue wave solutions. Indeed, the one-soliton was observed experimentally a decade ago [3] after it was predicted theoretically by Hasimoto [1].

Chapter 6

Conclusions and Further Work

The purpose of this dissertation was to model the formation and propagation of rogue waves on a vortex filament in both classical and quantum fluids, which is extremely relevant from the standpoint of quantum turbulence and superfluid vortex dynamics [13]. In a field that is as yet rather speculative and of great interest to current researchers, an understanding of the development of nonlinear rogue wave-like solutions in quantised vortices does indeed play a prominent role. The temporal decay typically expected from solutions such as the Peregrine soliton and the more generalised Akhmediev breather, has been well established from the results obtained in this dissertation.

The LIA model discussed throughout this study was sufficient to enable a comprehensive investigation of the local dynamics governing a single vortex filament in a classical/quantum fluid. This offers a suitable opportunity for further work to be carried out in relation to the interaction and reconnection of vortices using the non-local Biot-Savart model, to account for the effects of mutual interaction between neighbouring filaments in both classical and quantum fluids.

Another suggestion that might add to the present study would be to use the curvature and torsion results from Chapter 4 to generate Cartesian plots depicting the three-dimensional motion of vortex filaments in space using Section 2.4 and Appendix A. Finally, the ideas proposed for theoretical work would be incomplete, if sufficient experiments are not carried out to both confirm and validate the obtained results.

Appendix A

Calculation of the Position Curve from Curvature and Torsion

From the definition of $\mathcal{M}$ in Equation (2.39), it is possible to write

$$\exp(\mathcal{M}(s,t)) = \begin{bmatrix} M_{11}(s,t) & M_{12}(s,t) & M_{13}(s,t) \\ M_{21}(s,t) & M_{22}(s,t) & M_{23}(s,t) \\ M_{31}(s,t) & M_{32}(s,t) & M_{33}(s,t) \end{bmatrix}, \tag{A.1}$$

where the components of $\exp(M(s,t))$ are found to be

$$M_{11}(s,t) = \frac{\left(\int_0^s \kappa(\sigma,t)d\sigma\right)^2 \cos\left(\sqrt{\left(\int_0^s \kappa(\sigma,t)d\sigma\right)^2 + \left(\int_0^s \tau(\sigma,t)d\sigma\right)^2}\right) + \left(\int_0^s \tau(\sigma,t)d\sigma\right)^2}{\left(\int_0^s \kappa(\sigma,t)d\sigma\right)^2 + \left(\int_0^s \tau(\sigma,t)d\sigma\right)^2}, \tag{A.2}$$

$$M_{12}(s,t) = \frac{\left(\int_0^s \kappa(\sigma,t)d\sigma\right) \sin\left(\sqrt{\left(\int_0^s \kappa(\sigma,t)d\sigma\right)^2 + \left(\int_0^s \tau(\sigma,t)d\sigma\right)^2}\right)}{\sqrt{\left(\int_0^s \kappa(\sigma,t)d\sigma\right)^2 + \left(\int_0^s \tau(\sigma,t)d\sigma\right)^2}}, \tag{A.3}$$

$$M_{13}(s,t) = \frac{\left(\int_0^s \kappa(\sigma,t)d\sigma\right)\left(\int_0^s \tau(\sigma,t)d\sigma\right)\left[1 - \cos\left(\sqrt{\left(\int_0^s \kappa(\sigma,t)d\sigma\right)^2 + \left(\int_0^s \tau(\sigma,t)d\sigma\right)^2}\right)\right]}{\left(\int_0^s \kappa(\sigma,t)d\sigma\right)^2 + \left(\int_0^s \tau(\sigma,t)d\sigma\right)^2}, \tag{A.4}$$

$$M_{21}(s,t) = \frac{(\int_0^s \kappa(\sigma,t)d\sigma)\sin\left(\sqrt{(\int_0^s \kappa(\sigma,t)d\sigma)^2 + (\int_0^s \tau(\sigma,t)d\sigma)^2}\right)}{\sqrt{(\int_0^s \kappa(\sigma,t)d\sigma)^2 + (\int_0^s \tau(\sigma,t)d\sigma)^2}}, \tag{A.5}$$

$$M_{22}(s,t) = \cos\left(\sqrt{\left(\int_0^s \kappa(\sigma,t)d\sigma\right)^2 + \left(\int_0^s \tau(\sigma,t)d\sigma\right)^2}\right), \tag{A.6}$$

$$M_{23}(s,t) = \frac{(\int_0^s \tau(\sigma,t)d\sigma)\sin\left(\sqrt{(\int_0^s \kappa(\sigma,t)d\sigma)^2 + (\int_0^s \tau(\sigma,t)d\sigma)^2}\right)}{\sqrt{(\int_0^s \kappa(\sigma,t)d\sigma)^2 + (\int_0^s \tau(\sigma,t)d\sigma)^2}}, \tag{A.7}$$

$$\begin{aligned} M_{31}(s,t) = &\left(\int_0^s \kappa(\sigma,t)d\sigma\right)\left(\int_0^s \tau(\sigma,t)d\sigma\right) \\ &\times\left[1-\cos\left(\sqrt{\left(\int_0^s \kappa(\sigma,t)d\sigma\right)^2 + \left(\int_0^s \tau(\sigma,t)d\sigma\right)^2}\right)\right], \end{aligned} \tag{A.8}$$

$$M_{32}(s,t) = \frac{(\int_0^s \tau(\sigma,t)d\sigma)\sin\left(\sqrt{(\int_0^s \kappa(\sigma,t)d\sigma)^2 + (\int_0^s \tau(\sigma,t)d\sigma)^2}\right)}{\sqrt{(\int_0^s \kappa(\sigma,t)d\sigma)^2 + (\int_0^s \tau(\sigma,t)d\sigma)^2}}, \tag{A.9}$$

$$M_{33}(s,t) = \frac{(\int_0^s \kappa(\sigma,t)d\sigma)^2 + \cos\left(\sqrt{(\int_0^s \kappa(\sigma,t)d\sigma)^2 + (\int_0^s \tau(\sigma,t)d\sigma)^2}\right)}{(\int_0^s \kappa(\sigma,t)d\sigma)^2 + (\int_0^s \tau(\sigma,t)d\sigma)^2}. \tag{A.10}$$

Picking

$$\mathbf{C}(t) = \begin{bmatrix} c_{11}(t) & c_{12}(t) & c_{13}(t) \\ c_{21}(t) & c_{22}(t) & c_{23}(t) \\ c_{31}(t) & c_{32}(t) & c_{33}(t) \end{bmatrix}, \tag{A.11}$$

and using Equation (2.39), it is found that the matrix

$$\mathbf{W}(s,t) = \begin{bmatrix} \sum_{k=1}^{3} M_{1k}(s,t)c_{k1}(t) & \sum_{k=1}^{3} M_{1k}(s,t)c_{k2}(t) & \sum_{k=1}^{3} M_{1k}(s,t)c_{k3}(t) \\ \sum_{k=1}^{3} M_{2k}(s,t)c_{k1}(t) & \sum_{k=1}^{3} M_{2k}(s,t)c_{k2}(t) & \sum_{k=1}^{3} M_{2k}(s,t)c_{k3}(t) \\ \sum_{k=1}^{3} M_{3k}(s,t)c_{k1}(t) & \sum_{k=1}^{3} M_{3k}(s,t)c_{k2}(t) & \sum_{k=1}^{3} M_{3k}(s,t)c_{k3}(t) \end{bmatrix}. \tag{A.12}$$

Yet, recalling that

$$\mathbf{W}(s,t) = \begin{bmatrix} \mathbf{t}(s,t) \\ \mathbf{n}(s,t) \\ \mathbf{b}(s,t), \end{bmatrix}, \tag{A.13}$$

the tangent vector to the vortex filament curve $\mathbf{t}(s,t)$ must then be given by

$$\mathbf{t}(s,t) = \begin{bmatrix} \sum_{k=1}^{3} M_{1k}(s,t)c_{k1}(t) \\ \sum_{k=1}^{3} M_{1k}(s,t)c_{k2}(t) \\ \sum_{k=1}^{3} M_{1k}(s,t)c_{k3}(t). \end{bmatrix}, \tag{A.14}$$

Then from Equations (2.44) - (2.46), the position of the filament, in Cartesian coordinates, can be given by

$$\mathbf{r}(s,t) = \begin{bmatrix} \mathbf{x}(s,t) \\ \mathbf{y}(s,t) \\ \mathbf{z}(s,t), \end{bmatrix} = \begin{bmatrix} x_0(t) + \sum_{k=1}^{3} c_{k1}(t) \int_0^s M_{1k}(\sigma,t)d\sigma \\ y_0(t) + \sum_{k=1}^{3} c_{k2}(t) \int_0^s M_{1k}(\sigma,t)d\sigma \\ z_0(t) + \sum_{k=1}^{3} c_{k3}(t) \int_0^s M_{1k}(\sigma,t)d\sigma. \end{bmatrix}. \tag{A.15}$$

Thus, given curvature $\kappa(s,t)$ and torsion $\tau(s,t)$, the position of the vortex filament curve $\mathbf{r}(s,t)$ may always be recovered. It is therefore sufficient to study the curvature and torsion of the vortex filaments, as these quantities encode the salient geometric features of the curve $\mathbf{r}(s,t)$.

As an example, it is worth picking

$$\mathbf{C}(t) = \begin{bmatrix} 0 & 0 & 0 \\ 0 & 1 & -1 \\ 1 & 0 & 0 \end{bmatrix}, \tag{A.16}$$

and $x_0(t) = 0$, $y_0(t) = 0$, $z_0(t) = 1$.

Then, from the above analysis, the Cartesian coordinates of a vortex filament curve under these choices must take the form

$$x(s,t) = \int_0^s M_{13}(\hat{s},t)d\hat{s}, \tag{A.17}$$

$$y(s,t) = \int_0^s M_{12}(\hat{s},t)d\hat{s}, \tag{A.18}$$

$$z(s,t) = 1 - \int_0^s M_{12}(\hat{s},t)d\hat{s}. \tag{A.19}$$

Of course, many other examples can be constructed. Since the M_{ij} functions will depend on integrals of curvature and torsion, the form of these solutions will naturally vary depending on the specific solution $\psi(s,t) = \kappa(s,t)\mathrm{e}^{i\int_0^s \tau(\hat{s},t)d\hat{s}}$ chosen.

Bibliography

[1] H. Hasimoto. A soliton on a vortex filament. *Journal of Fluid Mechanics*, 51(3):477–485, 1972.

[2] R. A. Van Gorder. Quantum Hasimoto transformation and non-linear waves on a superfluid vortex filament under the quantum local induction approximation. *Physical Review E*, 91:053201, 2015.

[3] E.J. Hopfinger and F.K. Browand. Vortex solitary waves in a rotating, turbulent flow. *Nature*, 295:393–395, 1982.

[4] A. Chabchoub, N. P. Hoffmann, and N. Akhmediev. Rogue wave observation in a water wave tank. *Physical Review Letters*, 106:204502, 2011.

[5] R. A. Van Gorder. Orbital instability of the Peregrine soliton. *Journal of the Physical Society of Japan*, 83:054005, 2014.

[6] H. Salman. Breathers on quantized superfluid vortices. *Physical Review Letters*, 111:165301, 2013.

[7] R. L. Ricca. The contributions of Da Rios and Levi-Civita to asymptotic potential theory and vortex filament dynamics. *Fluid Dynamics Research*, 18:245–268, 1996.

[8] G.K. Batchelor. *An Introduction to Fluid Dynamics*. Cambridge University Press, 1967.

[9] L.S. Da Rios. On the motion of an unbounded liquid with a vortex filament of any shape. *Rendicoti del Circolo Matematico di Palermo*, 22:117–135, 1906.

[10] K. W. Schwarz. Three-dimensional vortex dynamics in superfluid He4: Line-line and line-boundary interactions. *Physical Review B*, 31:5782, 1985.

[11] R.P. Feynman. *Progress in Low Temperature Physics*, volume 1. North-Holland, Amsterdam, 1955.

[12] S. K. Nemirovskii and W. Fiszdon. Chaotic quantized vortices and hydrodynamic processes in superfluid helium. *Reviews of Modern Physics*, 67(1):37–84, 1995.

[13] S. K. Nemirovskii. Quantum turbulence: Theoretical and numerical problems. *Physics Reports*, 524(3):85–202, 2013.

[14] Lord Kelvin. On the vibrations of a columnar vortex. *Philosophical Magazine*, 5:155, 1880.

[15] A. Slunyaev, I. Didenkulova, and E. Pelinovsky. Rogue Waters. *Contemporary Physics*, 52:571–590, 2011.

[16] J. Brand and W. P. Reinhardt. Solitonic vortices and the fundamental modes of the "snake instability": Possibility of observation in the gaseous Bose-Einstein condensate. *Physical Review A*, 65:043612, 2002.

[17] M. J. Ablowitz. *Nonlinear Dispersive Waves: Asymptotic Analysis and Solitons*. Cambridge University Press, 2011.

[18] B. Kibler, J. Fatome, C. Finot, G. Millot, F. Dias, G. Genty, N. Akhmediev, and J. M. Dudley. The Peregrine soliton in nonlinear fibre optics. *Nature Physics*, 6:790–795, 2010.

[19] Y. V. Bludov, V. V. Konotop, and N. Akhmediev. Matter rogue waves. *Physical Review A*, 80:033610, 2009.

[20] H. Bailung, S. K. Sharma, and Y. Nakamura. Observation of Peregrine Solitons in a Multicomponent Plasma with Negative Ions. *Physical Review Letters*, 107:255005, 2011.

[21] J. S. Russell. Report on Waves. Report on 14th meeting, British Association for the Advancement of Science, 1844.

[22] P. G. Drazin and R. S. Johnson. *Solitons: an introduction*. Cambridge University Press, 1989.

[23] C. Kharif and E. Pelinovsky. Physical mechanisms of the rogue wave phenomenon. *European Journal of Mechanics*, 22:603–634, 2003.

[24] M. J. Ablowitz, D. J. Kaup, A. C. Newell, and H. Segur. Method for solving the sine-gordon equation. *Physical Review Letters*, 30(25):1262–1264, 1973.

[25] R.J. Arms and F. R. Hama. Localised-Induction Concept on a Curved Vortex and Motion of an Elliptic Vortex Ring. *Physics of Fluids*, 8(4):553–559, 1965.

[26] K.B. Dysthe and K. Trulsen. Note on Breather Type Solutions of the NLS as Models for Freak Waves. *Physica Scripta*, T82:48–52, 1999.

[27] B. K. Shivamoggi. Vortex Motion in Superfluid 4He: Effects of Normal Fluid Flow. *European Physical Journal B*, 86:275, 2013.

[28] R. A. Van Gorder. The Biot-Savart description of Kelvin waves on a quantum vortex filament in the presence of mutual friction and a driving fluid. *Proceedings of the Royal Society A*, 471:20150149, 2015.

[29] R. A. Van Gorder. Decay of helical Kelvin waves on a quantum vortex filament. *Physics of Fluids*, 26:075101, 2014.

[30] E. Fonda, D. P. Meichle, N. T. Ouellette, S. Hormoz, and D. P. Lathrop. Direct observation of Kelvin waves excited by quantized vortex reconnection. *Proceedings of the Natural Academy of Sciences*, 1:4707–4710, 2014.